Fluid Mechanics of Liquid Metal Batteries

Douglas H. Kelley
Department of Mechanical Engineering,
University of Rochester,
Rochester, NY 14627
e-mail: d.h.kelley@rochester.edu

Tom Weier
Institute of Fluid Dynamics,
Helmholtz-Zentrum Dresden-Rossendorf,
Bautzner Landstr. 400,
Dresden 01328, Germany
e-mail: t.weier@hzdr.de

The design and performance of liquid metal batteries (LMBs), a new technology for grid-scale energy storage, depend on fluid mechanics because the battery electrodes and electrolytes are entirely liquid. Here, we review prior and current research on the fluid mechanics of LMBs, pointing out opportunities for future studies. Because the technology in its present form is just a few years old, only a small number of publications have so far considered LMBs specifically. We hope to encourage collaboration and conversation by referencing as many of those publications as possible here. Much can also be learned by linking to extensive prior literature considering phenomena observed or expected in LMBs, including thermal convection, magnetoconvection, Marangoni flow, interface instabilities, the Tayler instability, and electro-vortex flow. We focus on phenomena, materials, length scales, and current densities relevant to the LMB designs currently being commercialized. We try to point out breakthroughs that could lead to design improvements or make new mechanisms important. [DOI: 10.1115/1.4038699]

1 Introduction

The story of fluid mechanics research in LMBs begins with one very important application: grid-scale storage. Electrical grids have almost no energy storage capacity, and adding storage will make them more robust and more resilient even as they incorporate increasing amounts of intermittent and unpredictable wind and solar generation. LMBs have unique advantages as a grid-scale storage technology, but their uniqueness also means that designers must consider chemical and physical mechanisms—including fluid mechanisms—that are relevant to few other battery technologies, and in many cases, not yet well-understood. We will review the fluid mechanics of LMBs, focusing on studies undertaken with that technology in mind, and also drawing extensively from prior work considering similar mechanisms in other contexts. In the interest of promoting dialogue across this new field, we have endeavored to include the work of many different researchers, though inevitably some would have eluded our search, and we ask for the reader's sympathy for regrettable omissions. Our story will be guided by technological application, focusing on mechanisms most relevant to LMBs as built for grid-scale storage. We will consider electrochemistry and theoretical fluid mechanics only briefly because excellent reviews of both topics are already available in the literature. In Sec. 1, we provide an overview and brief introduction to LMBs, motivated by the present state of worldwide electrical grids, including the various types of LMBs that have been developed. We consider the history of LMBs in more detail in Sec. 2, connecting to the thermally regenerative electrochemical cells developed in the middle of the twentieth century. Then, we consider the fluid mechanisms that are most relevant to LMBs: thermal convection and magnetoconvection in Sec. 3, Marangoni flow in Sec. 4, interface instabilities in Sec. 5, the Tayler instability in Sec. 6, and electro-vortex flow in Sec. 7. We conclude with a summary and reflection on future directions in Sec. 8.

A typical electrical grid spans a country or a continent, serving millions of consumers by linking them to an intricate network of hundreds or thousands of large generators. A grid can be understood as a single, gigantic machine, because all of its rotating generators must spin in synchrony, and within a fraction of a percent of their design speed, in order for the grid to function properly. Changes to any one part of the grid affect all parts of the grid. The implications of this interconnectedness are made more profound by the fact that today's grids have nearly zero storage capacity. When more electricity is being consumed than generated, the conservation of energy requires that the kinetic energy of the spinning generators drops, so they slow down, quickly losing synchrony, damaging equipment, and causing brownouts or blackouts if left unchecked. Conversely, when more electricity is being generated than consumed, generators speed up, risking all the same problems. Fluctuations in demand are as old as electrical utilities and have historically been managed by continually adjusting supply by turning generators on and off. Now, grids must also accommodate fluctuations in supply, as intermittent wind and solar generation expand rapidly because of their plummeting costs and the long-term imperative that humankind generate a significant share of our energy using renewable sources [1]. Large-scale storage on electrical grids would enable widespread deployment of renewable generation [2,3] while maintaining stability [4]. Many technologies for grid-scale storage have been proposed, including pumped hydro (which accounts for the vast majority of existing storage), pressurized air, thermal storage, flywheels, power-to-gas, and batteries. Liquid metal batteries (LMBs) are a particular grid-scale storage technology that comes with interesting fluid mechanical challenges.

Like any battery, a liquid metal battery discharges by allowing an energetically favorable chemical reaction to proceed in a controlled way. Control is maintained by separating the two reactants (the electrodes) with an electrolyte that prevents electrode materials from passing if they are neutral, but allows them to pass if they are ionized. Thus, the reaction proceeds only if some other path passes matching electrons, which then recombine with the ions and go on to react. The other path is the external circuit where useful work is done, thanks to the energy of the flowing electrons. The battery can later be recharged by driving electrons in the opposite direction, so that matching ions come along as well.

Battery electrodes can be made from a wide variety of materials, including liquid metals. For example, a liquid sodium negative electrode (anode) can be paired with a sulfur positive electrode (cathode) and a solid β-alumina electrolyte. (Here and throughout, we assign the names "anode" and "cathode" according to the roles played during discharge.) Na||S batteries operate at about 300 °C and have been deployed for grid-scale storage. ZEBRA batteries [5,6], named for the Zeolite Battery Research

Manuscript received September 14, 2017; final manuscript received November 27, 2017; published online January 31, 2018. Assoc. Editor: Jörg Schumacher.

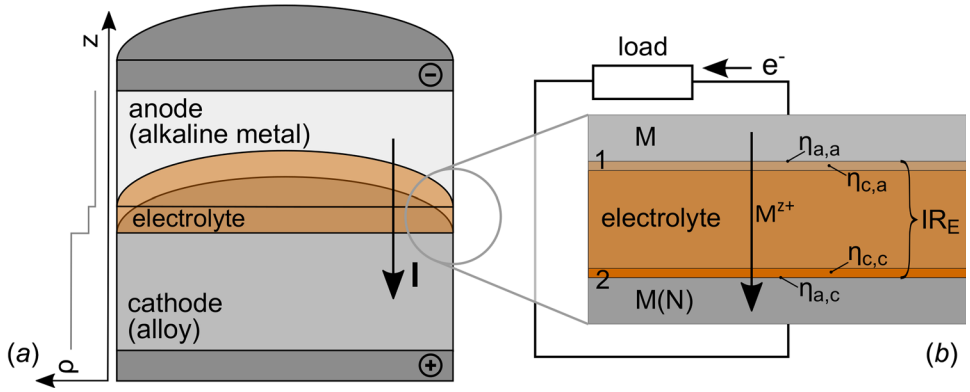

Fig. 1 Sketch of a liquid metal cell with discharge current and density profile for fully charged state and isothermal conditions (*a*) and schematic discharge process (*b*) from Ref. [12]

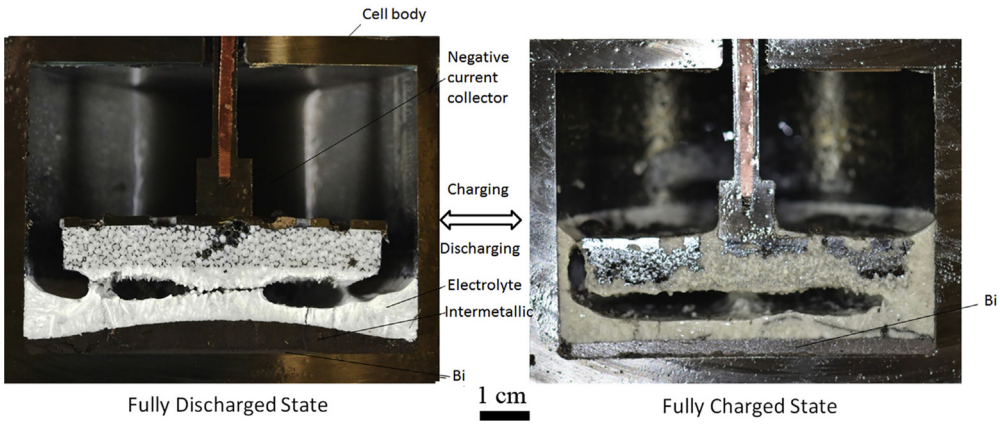

Fig. 2 Cross sections of prototype LMBs. Both are enclosed in a stainless steel casing that also serves as the positive current collector, and both have a foam negative current collector attached to a copper conductor that exits the top of the battery. In the discharged state (left), the foam is nearly filled with electrolyte, and a dark Li–Bi intermetallic layer is visible at bottom. In the charged state (right), lithium metal is visible in the foam, and the positive electrode at bottom has been restored to nearly pure bismuth. Because these photographs were taken at room temperature, the electrolyte does not fill the volume between the electrodes, but during operation, it would. The space above the negative current collector is filled with inert gas during operation. Adapted from Ref. [13], with permission.

Africa Project that developed them, use a $NaAlCl_4$ negative electrode that allows them to operate at temperatures as low as 245 °C. An electrolyte composed of Na-doped β-alumina conducts Na^+ ions. Lower operating temperatures are possible with batteries in which a Na negative electrode is combined with a $NiCl_2$ positive electrode and a $NaAlCl_4$ electrolyte, separated from the negative electrode with β-alumina to prevent corrosion. Alloying Cs with the Na can substantially improve wetting to β-alumina, allowing battery operation at still lower temperatures [7]. Sumitomo has recently documented a battery design using a eutectic mix of potassium and sodium bis(fluorosulfonyl)amide salts along with electrodes made from unspecified sodium compounds [8,9]. These battery designs and others like them involve liquid metals but require a solid separator between the layers.

As discovered at Argonne National Laboratory in the 1960s [10] and rediscovered at MIT recently [11], batteries can also be designed with liquid metal electrodes and molten salt electrolytes, requiring no separator at all. We shall use the term "liquid metal batteries" to refer to those designs specifically. An example is sketched in Fig. 1(*a*), and cross sections of two laboratory prototypes are shown in Fig. 2. The internal structure of the battery is maintained by gravity, since the negative electrode materials typically have lower density than electrolyte materials, which have lower density than positive electrode materials. A solid metal positive current collector contacts the positive electrode and usually serves as the container as well. A solid metal negative current collector connects to the negative electrode and is electrically insulated from the positive current collector.

Because the negative electrode is liquid and the positive current collector is also the battery vessel, some care is required to prevent shorts between them. It is possible to electrically insulate the positive current collector by lining it with a ceramic, but ceramic sleeves are too expensive for grid-scale applications and are prone to cracking. Instead, typical designs separate the liquid metal negative electrode from vessel walls with a metal foam, as shown in Fig. 2. The high surface tension of the liquid metal provides sufficient capillary forces to keep it contained in the pores of the foam. The solid foam also inhibits flow in the negative electrode, which is likely negligible at length scales larger than the pore size. In many designs, the foam is held in place by a rigid conductor, as shown, so that its height stays constant. However, as the battery discharges and the positive electrode becomes a pool of two-part alloy, it swells. If the positive electrode swells enough to contact the foam, a short occurs, so the foam height must be carefully chosen, taking into account the thickness of the positive electrode and the density change it will undergo during discharge.

Most liquid metal cells are concentration cells. Their open circuit voltage (OCV) is solely given by the activity of the alkaline metal in the cathode alloy. The equations for the transfer reactions at the two interfaces (see Fig. 1(*b*)) read

$$\mathrm{M} \rightarrow \mathrm{M}^{z+} + z\mathrm{e}^- \tag{1}$$

$$\mathrm{M}^{z+} + z\mathrm{e}^- \rightarrow \mathrm{M(N)} \tag{2}$$

for the anode/electrolyte interface (1) and the electrolyte/cathode interface (2) during discharge. M denotes an alkali ($z = 1$) or an earth-alkali ($z = 2$) metal of the negative electrode, and N refers to the heavy or half metal of the positive electrode. A variety of chemistries have been demonstrated, including Mg||Sb [14], Li||Pb–Sb [15], Li||Bi [13], Na|NaCl–$CaCl_2$|Zn [16,17], and Ca–Mg||Bi [18,19]. (See Ref. [20] for a review.) The Li||Pb–Sb chemistry has been studied most and is typically paired with a triple-eutectic LiF–LiCl–LiI electrolyte because of its relatively low melting temperature (about 341 °C [10,21]). The equilibrium potentials φ_0 of both half-cells can be written as

$$\varphi_0(1) = \varphi_{00} + \frac{\mathrm{RT}}{zF} \ln \frac{a_{\mathrm{M}^{z+}}}{a_{\mathrm{M}}} \tag{3}$$

$$\varphi_0(2) = \varphi_{00} + \frac{\mathrm{RT}}{zF} \ln \frac{a_{\mathrm{M}^{z+}}}{a_{\mathrm{M(N)}}} \tag{4}$$

with the standard potential φ_{00}, the universal gas constant R, the temperature T, the Faraday constant F, and the activity a of the metal in the pure (M), the ionic (M^{z+}), and the alloyed (M(N)) state. The difference of the two electrode potentials $\varphi_0(2)$ and $\varphi_0(1)$ is the cell's OCV

$$E_{\mathrm{OC}} = -\frac{\mathrm{RT}}{zF} \ln a_{\mathrm{M(N)}} \tag{5}$$

Only the activity of the alkali metal in the alloy $a_{\mathrm{M(N)}}$ determines the OCV since the standard potentials of both half cells are identical and the activity of the pure anode is one by definition. Under current flow, only the terminal voltage E is available. It is the difference of OCV and several terms describing voltage losses, i.e., polarizations (cf. [22] and Fig. 1(*b*)) occurring under current (I) flow

$$E = E_{\mathrm{OC}} - IR_E - \eta_{c,a} - \eta_{c,c} - \eta_{a,a} - \eta_{a,c} \tag{6}$$

These voltage losses are due to the electrolyte resistance R_{E}, the concentration polarizations at the anode $\eta_{c,a}$ and cathode $\eta_{c,c}$, and the corresponding activation potentials $\eta_{a,a}$ and $\eta_{a,c}$. Typically, ohmic losses dominate activation and concentration polarizations by far, but mass transfer limitations may nevertheless sometimes occur in the cathodic alloy.

Liquid metal batteries have advantages for grid-scale storage. Eliminating solid separators reduces cost and eliminates the possibility of failure from a cracked separator. Perhaps more importantly, solid separators typically allow much slower mass transport than liquids, so eliminating solids allows faster charge and discharge with smaller voltage losses. Liquid electrodes improve battery life, because the life of Li-ion and other more traditional batteries is limited when their solid electrodes are destroyed due to repeated shrinking and swelling during charge and discharge. Projections from experimental measurements predict that Li||Pb–Sb batteries will retain 85% of their capacity after daily discharge for ten years [15]. The Li||Pb–Sb chemistry is composed of Earth-abundant elements available in quantities large enough to provide many GWh of storage. Low cost is also critical if a technology is to be deployed widely [23], and liquid metal batteries are forecast to have costs near the $100/kWh target set by the U.S. Advanced Research Projects Agency-Energy (ARPA-e). Their energy and power density are moderate, and substantially below the Li-ion batteries that are ubiquitous in portable electronics, but density is less essential than cost in stationary grid-scale storage. Li-ion batteries today cost substantially more than $100/kWh, but their costs have dropped continually over time and will likely drop substantially more as the Tesla GigaFactory 1, the world's largest Li-ion battery plant, continues to increase its production. The energy efficiency of liquid metal batteries varies widely with current density, but at a typical design value of 275 mA/cm^2 is 73% [15], similar to pumped hydro storage.

Liquid metal batteries also present challenges. During discharge, Li||Pb–Sb batteries provide only about 0.8 V [15]. Despite variation with battery chemistry, all conventional liquid metal batteries have voltage significantly less than Li-ion batteries. Lacking solid separators, liquid metal batteries are not suitable for portable applications in which disturbing the fluid layers could rupture the electrolyte layer, causing electrical shorts between the positive and negative electrodes and destroying the battery. Rupture might also result from vigorous fluid flows even if the battery is stationary, such as the Tayler instability (Sec. 6), interface instabilities (Sec. 5), Marangoni flow (Sec. 4), electro-vortex flow (Sec. 7), or their combination. Flow mechanisms may also interact, triggering instabilities more readily. The existing liquid metal battery chemistries require high operating temperatures (475 °C for Li||Pb–Sb). Little energy is wasted heating large batteries because Joule heating (losses to electrical resistance) provides more than enough energy to maintain the temperature. Still, high temperatures promote corrosion and make air-tight mechanical seals difficult. Finally, poor mixing during discharge can cause local regions of a liquid metal electrode to form unintended intermetallic solids that can eventually span from the positive to the negative electrode, destroying the battery. Solid formation may well be the leading cause of failure in liquid metal batteries.

2 History and Past Work

2.1 Three-Layer Aluminum Refinement Cells. The central idea at the heart of LMBs is the three-layer arrangement of liquid electrodes and electrolyte. This seemingly simple idea (in fact so apparently simple that it is sometimes [24] questioned if it deserves to be patented at all) did not originate with LMBs. Instead, using a stable stratification of two liquid metals interspaced with a molten salt for electrochemical purposes was first proposed 1905 by Betts [25] in the context of aluminum purification (see Fig. 3(*b*)). However, Betts was not able to commercialize his process. Instead Hoopes, who had a more complicated arrangement using a second internal vessel for aluminum electrorefining patented in 1901 [26] (Fig. 3(*a*)), developed later a water-cooled three-layer cell [27] (Fig. 3(*c*)) that could be successfully operated. According to Frary [28], Hoopes as well thought of using a three-layer cell around 1900. It can be seen from Table 1 that even if the idea to use three liquid layers were a trivial one, its realization and transformation to a working process was highly nontrivial indeed.

The submerged vessel containing the negative electrode, initially suggested by Hoopes [26] (Fig. 3(*a*)), is filled with molten impure aluminum and surrounded by a bath of fused cryolite. Cryolite is less dense than the pure or impure Al. In the presence of flow, Al dissolves into the cryolite and deposits at the carbon walls of the outer vessel, and pure Al can be collected at the bottom of the outer vessel. However, the current density is distributed very inhomogeneously, concentrating around the opening of the inner vessel. This implies large energy losses and strong local heating rendering a stable operation over longer times impossible.

Betts [25,29] (Fig. 3(*b*)) alloyed the impure Al with Cu and added BaF_2 to the cryolite to increase the density of the salt mixture and to enable the purified Al to float on the fused salt. This three-layer arrangement guaranteed the shortest possible current

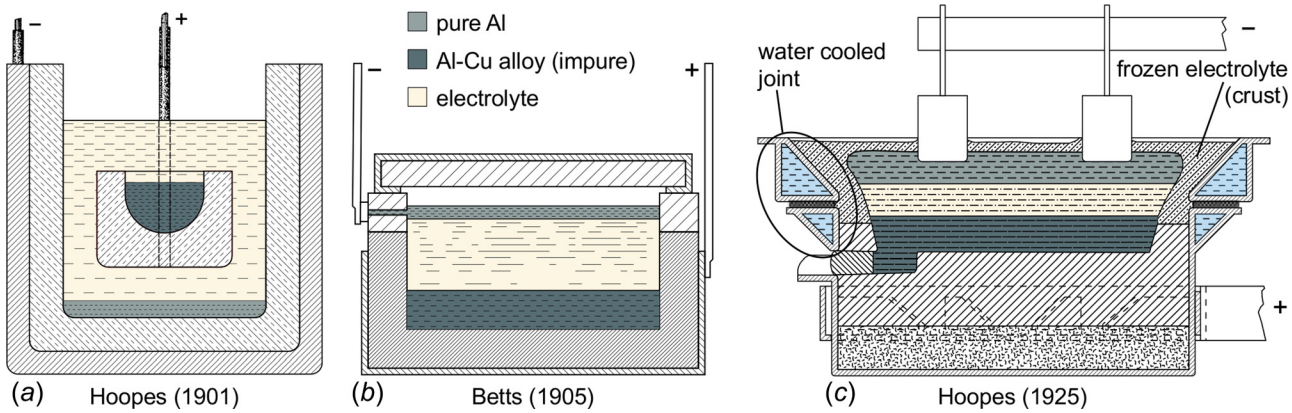

Fig. 3 Aluminum refinement cells adapted from Hoopes [26] (*a*), Betts [25] (*b*), and Drossbach [24] (*c*)

Table 1 Characteristics of different three-layer aluminum refining processes (approximate values, adapted from Table I of Ref. [38] and Table 6 of Ref. [34])

	Hoopes process	Gadeau process	S.A.I.A. process
Top layer	Pure Al	Pure Al	Pure Al
Density/kgm^{-3}	2290	2300	2300
Melting point/°C	660	660	660
Electrolyte	AlF_3–NaF–BaF_2	AlF_3–NaF–$BaCl_2$–NaCl	AlF_3–NaF–BaF_2–CaF_2
Composition (mass%)	0.34–0.28–0.38	0.15–0.17–0.6–0.08	0.48–0.18–0.18–0.16
Density/kgm^{-3}	2500	2700	2500
Melting point/°C	900	700	670
Bottom layer	Al–Cu	Al–Cu–Other	Al–Cu
Composition (mass%)	0.75–0.25	0.6–0.28–0.12	0.7–0.3
Density/kgm^{-3}	2800	3140	3050
Melting point/°C	550	Unspecified	590
Operating temperature/°C	950	800	750

paths and enabled homogeneous current density distributions. Additionally, the evaporation of the electrolyte was drastically reduced by the Al top layer. However, under the high operating temperatures the cell walls became electrically conducting, got covered with metal that short-circuited the negative and positive electrodes, and thus, prevented successful operation of the cell [29].

Only Hoopes' sophisticated construction [27,28] (Fig. 3(*c*)) was finally able to operate for longer times. A key element of Hoopes' construction is the division of the cell into two electrically insulated sections. The joint between them is water cooled and thereby covered by a crust of frozen electrolyte providing electrical as well as thermal insulation [30]. A similar idea was later applied to Na||Bi galvanic cells by Shimotake and Hesson [31]. Additionally, instead of using a single electric contact to the purified Al at the cells' side as did Betts, Hoopes arranged several graphite current collectors along the Al surface that provided a more evenly distributed current. However, the electrolyte used by Hoopes (see Table 1) had a relatively high melting temperature and a tendency to creep to the surface between the cell walls and the purified Al [28,32]. According to Eger [33] and Beljajew et al. [34] (see as well Gadeau [35]), the complicated design of Hoopes' cell, especially the water cooled walls, prevented continuous use in production. It was not until 1934 that super-purity aluminum became widely available with Gadeau's [36] three-layer refining process that used a different electrolyte (see Table 1) according to a patent filed in 1932. Its lower melting point allowed for considerably decreased operating temperature. Gadeau's cell was lined with magnesite that could withstand the electrolyte attack without the need of water cooling. However, the $BaCl_2$ used in the electrolyte mixture decomposed partially, so the electrolyte composition had to be monitored and adjusted during cell operation when necessary. This difficulty was overcome by using the purely fluoride-based electrolyte composition suggested by Hurter [37] (see Table 1, S.A.I.A. process).

Aluminum refining cells can tolerate larger voltage drops than LMBs, so the electrolyte layer is often much thicker. Values quoted are between 8 cm [34,39] that should be a good estimate for current practice [40], 10 cm [32], 20 cm [41], and 25 cm [38]. These large values are, on the one hand, due to the need for heat production. On the other hand, a large distance between the negative and positive electrodes is necessary to prevent flow induced intermixing of the electrode metals that would nullify refinement. It is often mentioned [28,32,38,42] that strong electromagnetic forces trigger those flows. Unlike aluminum electrolysis cells (ACEs), refinement cells have been optimized little, and the technology would certainly gain from new research [41]. Yan and Fray [41] directly invoke the low density differences as a cause for the instability of the interfaces, discussed here in Sec. 5. They attribute the limited application of fused salt electrorefining to the present design of refining cells that does not take advantage of the high electrical conductivity and the very low thermodynamic potential required for the process. Coupling optimized electrorefining to carbon-free generation of electricity should, according to Yan and Fray [41], result in "greener" metallurgy.

The application of three-layer processes was also proposed for electronic scrap reclamation [43], removal of Mg from scrap Al [44–46], and electrorefining of Si [47–49]. Research on the fluid mechanics of current bearing three-layer systems can, therefore, potentially be useful beyond LMBs.

2.2 Thermally Regenerative Electrochemical Systems. After three-layer liquid metal systems were put to use for Al

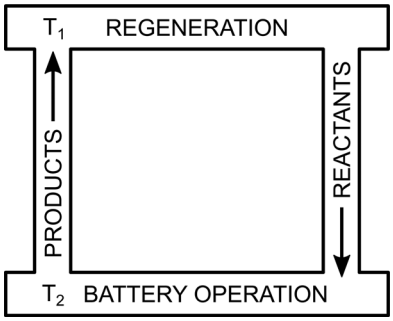

Fig. 4 Closed cycle battery system suggested by Yeager in 1957, adapted from Roberts [50]

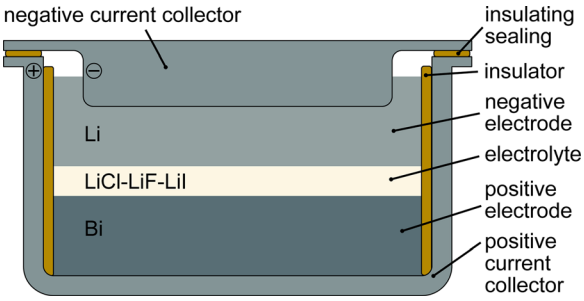

Fig. 5 Sketch of a differential density cell

refining, a few decades passed before they were used to generate electricity. In the meantime, related technologies were developed, including "closed cycle battery systems" (Yeager in Ref. [50]), "thermally regenerative fuel cells" or "(thermally) regenerative electrochemical systems (TRES)" as they were later subsumed by Liebhafsky [51], McCully et al. [52], and Chum and Osteryoung [53,54]. TRES combine an electricity delivering cell with a regeneration unit as sketched in Fig. 4: reactants are combined at the low cell temperature T_2, and then the product is thermally decomposed at the higher regenerator temperature T_1. Thermal regeneration implies that the whole system efficiency is Carnot limited [55,56].

A variety of such systems were investigated in the U.S. during the period of 1958–1968 [53]. Later, Chum and Osteryoung classified the published material on this topic according to system type and thoroughly reviewed it in retrospect [53,54]. LiH-based cells were building blocks of what were probably the first (1958, [53]) experimentally realized thermally regenerative high-temperature systems [57–59], which continue to be of interest today [60,61]. Almost at the same time a patent was filed in 1960 by Agruss [62], bimetallic cells were suggested for the electricity delivering part of TRES. Henderson et al. [63] concluded their survey of some 900 inorganic compounds for use in thermally regenerative fuel cell systems with the recommendation to concentrate on minimizing electrochemical losses, i.e., polarization and resistance losses, in order to increase overall efficiency. Although unmentioned in Ref. [63], bimetallic cells with liquid metal electrodes and fused salt electrolytes were deemed most suitable to fulfill those requirements [64]. Governmental sponsored research on bimetallic cells followed soon after at Argonne National Laboratory (1961, [65]) and at General Motors (1962 [64,66]). Research was initially focused on the application of bimetallic cell based TRES on space power applications [67], namely, systems using nuclear reactors as heat sources. Several studies explored the parameters of concrete designs developed in the frame of "systems nuclear auxiliary power program" (SNAP), SNAP-2 [67–71] and SNAP-8 [54].

Hydrodynamics naturally plays a vital role in the operation of TRES due to the necessity to transport products and reactants between the electricity producing and the thermal regeneration parts of the system. However, hydrodynamics of the transport between the cell and the regenerator is mainly concerned with the task of pumping [69,71] and the subtleties of keeping a liquid metal flow through—while preventing electrical contact between—different cells [67]. Velocities typical for TRES are much lower than those found in conventional heat engines [72] and could even be achieved using natural circulation driven by heat [10]. Agruss et al. [67] emphasized that the solutal convection should be taken into account when designing TRES cells and the flow control is vital to obtain good long-term performance. Publications covering detailed investigations of cell specific fluid mechanics are unknown to the present authors, but the LMB pioneers were obviously aware of its importance as can be seen by a variety of pertinent notes.

Cell construction determines to a large extent the influence hydrodynamics can have on cell operation. No mechanical obstructions exist in "differential density cell" [54,67–69] sketched in Fig. 5. This is most likely the purest embodiment of an LMB: inside the cell, there are only the three fluid layers that are floating on top of each other according to density. Early on, the vital role of stable density stratification was clearly identified [54,69,73]. The interfaces of differential density cells using a K|KOH–KBr–KI|Hg system were stable enough to allow for a mild Hg feed of a few milliliters per minute [67]. Cell performance depended on the flow distribution, the volume flux, and, vicariously, on the temperature of the incoming Hg. Cairns et al. [10] presented a conceptual design for a battery of three Na|NaF–NaCl–NaI|Bi differential density cells, stressed that the density differences are large enough to clearly separate the phases, and mentioned in the same breath that "hydrodynamic stability of the liquid streams must be carefully established."

Restraining one or more of the liquid phases in a porous ceramic matrix is a straightforward means to guarantee mechanical stability of the interfaces [22]. A direct mechanical separation of anodic and cathodic compartment is a necessity for space applications that could not rely on gravity to keep the layers apart. Besides the solid matrix, another means to immobilize electrolytes was to intermix them with ceramic powders, the so-called "fillers," that resulted in paste electrolytes. Since both matrix and powders had to be electric insulators, an overall conductivity reduction by a factor of about two to four [74,75] resulted even for the better paste electrolytes. Obviously, using mechanically separated electrode compartments is a prerequisite for any mobile application of LMBs. Equally, for cells used as components in complete TRES, the constant flow to and from the regenerator and through the cell necessitates in almost all cases a mechanical division of positive and negative electrodes. Examples include the flow through cell with sandwich matrix by Agruss and Karas [69], the earlier single cup cell of "flowing type" using an electrolyte impregnated alumina thimble [68], and the paste electrolyte cells developed at Argonne National Laboratory [74,76].

A different purpose was pursued by encasing the negative electrode material into a retainer [77] made from stainless steel fibers [10], felt metal [78], or later, foam [13,15,19,79] as sketched in Fig. 6. Those retainers allow electrical insulation of the negative electrode from the rest of the cell without resorting to ceramics and restrict fluid mechanics to that in a porous body. The probably simplest retainer used was an Armco iron ring [10,65] that encased the alkaline metal, a configuration more akin to the differential density cell than to a porous body. Arrangements similar to the iron ring are sometimes used as well in molten salt electrolysis cells [27,33,80,81] to keep a patch of molten metal floating on top of fused salt while preventing contact with the rest of the cell. In the case of poorly conducting materials (especially Te and Se), the positive electrode had to be equipped with additional

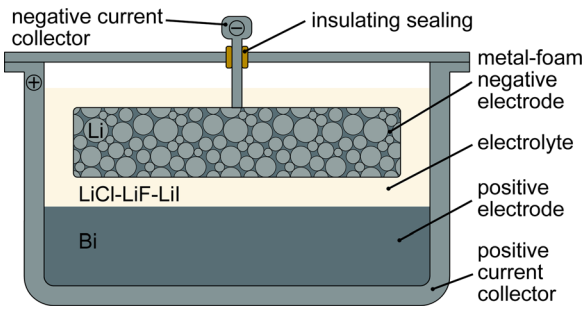

Fig. 6 Sketch of a liquid metal cell featuring a retainer (metal foam) to contain the negative electrode

electronically conducting components to improve current collection [22,76].

With view on the low overall efficiencies of TRES due to Carnot cycle limitations as well as problems of pumping, plumbing, and separation, research on thermally regenerative systems ceased after 1968 [54] and later LMB work at Argonne concentrated on Li-based systems with chalcogen positive electrodes, namely, Se and Te. The high strength of the bonds in those systems makes them unsuitable for thermal regeneration [22]. However, in their review, Chum and Osteryoung [54] deemed it worthwhile to reinvestigate TRES based on alloy cells once a solar-derived, high temperature source was identified. Just recently, a Na||S-based approach for solar electricity generation using thermal regeneration was suggested [82].

2.3 Liquid Metal Batteries for Stationary Storage. Using bimetallic cells as secondary elements for off-peak electricity storage was already a topic in the 1960s [10,83]. The very powerful Li||Se and Li||Te cells [75] mentioned above are, however, unsuitable for wide scale use because of the scarcity of the both chalcogens [22,84,85]. In the late 1960s and early 1970s, research at Argonne moved on to Li||S [22,85–87], thus leaving the area of bimetallic cells.

LMB activities were reinvigorated at MIT in the first years of the 21st century by Donald Sadoway. The initial design conceived in the fall of 2005 by Sadoway and Ceder and presented by Bradwell [88] was one that combined Mg and Sb with a Mg_3Sb_2-containing electrolyte, decomposing the Mg_3Sb_2 on charge and forming it on discharge. This new cell design was later termed "Type A" or "ambipolar electrolysis LMB" [89] and not followed up later. Instead, bimetallic alloying cells ("Type B") were investigated using different material combinations whose selection was not hampered by the need of thermal regeneration. The Mg||Sb system was among the first alloying systems studied at MIT. With $MgCl_2$–NaCl–KCl (50:30:20 mol%), it used a standard electrolyte for Mg electrolysis [90]. Thermodynamic data for the system are available from Ref. [91] and cell performance data were later reported also by Leung et al. [92].

Right from the start, research at MIT focused on the deployment of LMBs for large-scale energy storage [14] concentrating on different practical and economical aspects of utilizing abundant and cheap materials [18,23]. Initially, large cells with volumes of a few cubic meters [93] and cross sections of (>2 m × 2 m) [88] were envisioned. Those cells would have a favorable volume to surface ratio translating into a small amount of construction material per active material and potentially decreasing total costs. In addition, in large cells, Joule heating in the electrolyte could be sufficient to keep the components molten [14].

The differential density cells employed for the initial MIT investigations gave later way to cells that used metal foam immersed in the electrolyte to contain the negative electrode [13,15,19,79,94].

Successful scaling on the cell level from 1 cm diameter to 15 cm diameter was demonstrated by Ning et al. [13]. Commercial cells produced by the MIT spin-off Ambri have square cross sections of 10 cm and 20 cm edge length [95]. Thus, state-of-the-art cells are moderately sized, but the quest for large-scale cells is ongoing. Recently, Bojarevics and coworkers [96,97] suggested to retrofit old aluminum electrolysis potlines into large-scale LMB installations ending up with cells of 8 m by 3.6 m cross section and about 0.5 m total liquid height.

It should be stressed that LMBs form a whole category of battery systems comprising a variety of material combinations. Consequently, depending on the active materials and the electrolyte selected, different flow situations may arise even under identical geometrical settings.

3 Thermal Convection and Magnetoconvection

Because almost every known fluid expands when heated, spatial variations (gradients) in temperature cause gradients in density. In the presence of gravity, if those gradients are large enough, denser fluid sinks and lighter fluid floats, causing thermal convection. Usually, large-scale convection rolls characterize the flow shape. Being ubiquitous and fundamental in engineering and natural systems, convection has been studied extensively, and many reviews of thermal convection are available [98–101]. Here, we will give a brief introduction to convection, then focus on the particular characteristics of convection in liquid metal batteries. Joule heating drives convection in some parts of a liquid metal battery, but inhibits it in others. Broad, thin layers are common, and convection in liquid metal batteries differs from aqueous fluids because metals are excellent thermal conductors (that is, they have low Prandtl number). Convection driven by buoyancy also competes with Marangoni flow driven by surface tension, as discussed in Sec. 4. We close this section with a discussion of magnetoconvection in which the presence of magnetic fields alters convective flow.

3.1 Introduction to Thermal Convection. Thermal convection is driven by gravity, temperature gradients, and thermal expansion, but hindered by viscosity and thermal diffusion. Convection also occurs more readily in thicker fluid layers. Combining these physical parameters produces the dimensionless Rayleigh number

$$\mathrm{Ra} = \frac{g\alpha_T \Delta T L^3}{\nu\kappa}$$

where g is the acceleration due to gravity, α_T is the coefficient of volumetric expansion, ΔT is the characteristic temperature difference, L is the vertical thickness, ν is the kinematic viscosity, and κ is the thermal diffusivity. The Rayleigh number can be understood as a dimensionless temperature difference and a control parameter; for a given fluid and vessel shape, convection typically begins at a critical value $\mathrm{Ra} > \mathrm{Ra}_{\mathrm{crit}} > 0$, and subsequent instabilities that change the flow are also typically governed by Ra.

If the Rayleigh number is understood as a control parameter, then the results of changing Ra can also be expressed in terms of dimensionless quantities. The Reynolds number

$$\mathrm{Re} = \frac{UL}{\nu} \tag{7}$$

where U is a characteristic flow velocity, can be understood as a dimensionless flow speed. The Nusselt number

$$\mathrm{Nu} = -\frac{QL}{\kappa c_p \rho \Delta T}$$

Table 2 Properties of common electrode materials. Values for metals at respective melting temperature taken from Refs. [103] and [104] except Li conductivity from Ref. [105], Pb–Bi eutectic data from Sobolev [106], and Pb data from Ref. [102].

Material	$\nu/10^{-6}$ (m^2/s)	$\kappa/10^{-5}$ (m^2/s)	ρ (kg/m^3)	$\alpha_T/10^{-4}$ (K^{-1})	$\sigma_E/10^6$ (S/m)	Pr	Pm/10^{-6}
Negative electrode							
Li	1.162	2.050	518	1.9	3.994	0.0567	5.8315
Mg	0.7862	3.4751	1590	1.6	3.634	0.0226	3.5907
Na	0.7497	6.9824	927	2.54	10.42	0.0107	9.8195
Positive electrode							
Bi	0.1582	1.1658	10,050	1.17	0.768	0.0136	0.1527
Pb	0.253	1.000	10,673	1.199	1.050	0.0253	0.334
Sb	0.2221	1.3047	6483	1.3	0.890	0.0170	0.2485
Zn	0.5323	1.5688	6575	1.5	2.67	0.0339	1.7860
Eutectic Pb–Bi	0.3114	0.5982	10,550	1.22	0.909	0.052	0.3557

where Q is the total heat flux through the fluid, c_p is the specific heat at constant pressure, and ρ is the mass density, can be understood as a dimensionless heat flux.

The canonical and best-studied context in which convection occurs is the Rayleigh–Bénard case, in which a fluid is contained between upper and lower rigid, no-slip boundaries, with the lower boundary heated and the upper boundary cooled. Usually, both boundaries are held at steady, uniform temperatures, or subjected to steady, uniform heat flux. Convection also occurs in many other geometries, for example, lateral heating. Heating the fluid from above, however, produces a stably stratified situation in which flow is hindered.

3.2 Introduction to Compositional Convection. Temperature is not the only parameter that affects fluid density. Chemical reactions, for example, can also change the local density such that buoyancy drives flow. That process is known as compositional convection, and the corresponding control parameter is the compositional Rayleigh number

$$\mathrm{Ra}_X = \frac{g\alpha_X \Delta X L^3}{\nu D}$$

where α_X is the coefficient of volumetric expansion with concentration changes, ΔX is the characteristic concentration difference, and D is the material diffusivity. (Compositional convection is one mechanism by which reaction drives flow; entropic heating, discussed earlier, is another.) For liquid metal batteries, the electrode materials have densities that differ by more than an order of magnitude (see Table 2), and $\Delta X \sim 30$ mol %, so we expect compositional convection to cause substantial flow. For comparison, we can consider thermal convection in bismuth at 475 °C for which the coefficient of thermal expansion is $\alpha_T = 1.24 \times 10^{-4}$/K [102]. Making the order-of-magnitude estimate $\Delta T \sim 1$ K, it becomes clear that $\alpha_X \Delta X \gg \alpha_T \Delta T$. For the Na||Bi system at an operating temperature of 475 °C, the compositional Rayleigh number exceeds the thermal one by six orders of magnitude. Thus, compositional convection is likely much stronger than thermal convection. Compositional convection is unlikely during discharge because the less-dense negative electrode material (e.g., Li) is added to the top of the more-dense positive electrode, producing a stable density stratification. During charge, however, less-dense material is removed from the top of the positive electrode, leaving the remaining material more dense and likely to drive compositional convection by sinking.

3.3 Metals and Salts: Convection at Low Prandtl Number. In addition to the Rayleigh number, a second dimensionless parameter specifies the state of a convecting system, the Prandtl number

$$\mathrm{Pr} = \frac{\nu}{\kappa}$$

A ratio of momentum diffusivity (kinematic viscosity) to thermal diffusivity, the Prandtl number, is a material property that can be understood as a comparison of the rates at which thermal motions spread momentum and heat. Table 2 lists the Prandtl number of a few relevant fluids. Air and water are very often the fluids of choice for convection studies, since so many industrial and natural systems involve them. But air and water have Prandtl numbers that differ from liquid metals and molten salts by orders of magnitude: $\mathrm{Pr} = 7$ for water and $\mathrm{Pr} = 0.7$ for air. We therefore expect thermal convection in liquid metals and molten salts to differ substantially from convection in water or air.

The Prandtl number plays a leading role in the well-known scaling theory characterizing turbulent convection, developed by Grossmann and Lohse [107]. In fact, the scaling theory expresses the outputs Re and Nu in terms of the inputs Ra and Pr. To begin, every possible Rayleigh–Bénard experiment is categorized according to the role of boundary layers in transporting momentum and heat. Boundary layers occur near walls, and transport through them proceeds (to a good approximation) by diffusion alone. On the other hand, in the bulk region far from walls, transport proceeds primarily by the fast and disordered motions typical in turbulent flow. Any particular Rayleigh–Bénard experiment can be assigned to one of eight regimes, depending on three questions: Is momentum transport slower through the boundary layer or the bulk? Is heat transport slower through the boundary layer or the bulk? And, which boundary layer—viscous or thermal—is thicker and therefore dominant? Answering those three questions makes it possible to estimate the exponents that characterize the dependence of Re and Nu on Ra and Pr. According to the theory [107], the Nusselt number can depend on the Prandtl number as weakly as $\mathrm{Nu} \propto \mathrm{Pr}^{-1/12}$ or as strongly as $\mathrm{Nu} \propto \mathrm{Pr}^{1/2}$, and the Reynolds number can depend on the Prandtl number as weakly as $\mathrm{Re} \propto \mathrm{Pr}^{-1/2}$ or as strongly as $\mathrm{Re} \propto \mathrm{Pr}^{-6/7}$. Again, convection in liquid metals and molten salts differs starkly from convection in water or air: changing Pr by orders of magnitude causes Re and Nu to change by orders of magnitude as well. Experiments studying convection in sodium ($\mathrm{Pr} = 0.0107$) have confirmed that the heat flux (Nu) for a given temperature difference (Ra) is indeed smaller than for fluids with larger Pr [108]. Experiments have also shown that at low Pr, more of the flow's kinetic energy is concentrated in large-scale structures, especially large convection rolls. In a thin convecting layer with a cylindrical sidewall resembling the positive electrode of a liquid metal battery, slowly fluctuating concentric ring-shaped rolls often dominate [108]. Those rolls may interact via flywheel effects [109].

3.4 Magnetoconvection. Convection in liquid metal batteries proceeds in the presence of—and can be substantially altered by—electric currents and magnetic fields. Introductions and overviews of the topic of magnetoconvection have been provided in texts dedicated to the subject [110] as well as texts on the more general topic of magnetohydrodynamics [111]. The strength of

the magnetic field can be represented in dimensionless form using the Hartmann number

$$\mathrm{Ha} = BL\sqrt{\frac{\sigma_E}{\rho\nu}} \tag{8}$$

which is the ratio of electromagnetic force to viscous force. Here, B is the characteristic magnetic field strength and σ_E is the electrical conductivity. (Magnetic field strength is also sometimes expressed using the Chandrasekhar number, which is the square of the Hartmann number.) When $\mathrm{Ha} \gg 1$, magnetic fields tend to strongly alter convection, though the particular effects depend on geometry. Often, convection rolls align with magnetic field lines, in broad analogy to the tendency of charged particles to orbit magnetic field lines. Other motions, such as helical paths, are also possible.

If convection occurs in the presence of a vertical magnetic field, alignment is impossible, since convection rolls are necessarily horizontal. Accordingly, vertical magnetic fields tend to damp convection [112–114]. The critical Rayleigh number at which convection begins scales as $\mathrm{Ra}_{\mathrm{crit}} \propto \mathrm{Ha}^2$ [112], as has been verified experimentally [115]. The Rayleigh number of oscillatory instability of convection rolls is also increased by the presence of a vertical magnetic field [113]. Common sources of vertical magnetic fields in liquid metal batteries include the Earth's field (though it is relatively weak) and fields produced by wires carrying current to and from the battery.

Just as the Grossmann and Lohse scaling theory [107] considers the dependence of Re and Nu on the inputs Ra and Pr in convection without magnetic fields, a recent scaling theory by Schumacher and colleagues [116] considers the dependence of Re and Nu on the inputs Ra, Pr—and also Ha—in the presence of a vertical magnetic field. The reasoning is analogous: the scaling depends on whether transport time is dominated by the boundary layer or the bulk, and which boundary layer is thickest. However, the situation is made more complex by the need to consider magnetic field transport in addition to momentum and temperature transport, and the possibility that the Hartmann (magnetic) boundary layer might be thickest. Altogether, 24 regimes are possible. To reduce the number of free parameters, the authors considered the case in which $\mathrm{Pr} \ll 1$ and $\mathrm{Pm} \ll 1$, where $\mathrm{Pm} = \nu\mu\sigma_E$ is the magnetic Prandtl number. (Here, μ is the magnetic permeability.) That special case applies to materials common in liquid metal batteries and still spans four regimes of magnetoconvection. Categorization depends on whether the magnetic field is strong ($\mathrm{Ha} \gg 1$) and whether the flow is substantially nonlinear ($\mathrm{Ra} \gg 1$). Scaling laws are proposed for each regime. The theory's fit parameters remain unconstrained in three of the four regimes because appropriate experimental data are unavailable. Experiments to produce those data would substantially advance the field.

On the other hand, if a horizontal magnetic field is present, convection rolls are often able to align with it easily. In that case, flow speed (Re) and heat flux (Nu) increase [117]. Moreover, since magnetic fields of any orientation damp turbulence [118], convection in the presence of horizontal magnetic fields tends to be more ordered, spatially, than convection in the $\mathrm{Ha} = 0$ case. As Ra increases, waves develop on the horizontal convection rolls [108,113,119].

In liquid metal batteries, internal electrical currents run primarily vertically and induce toroidal horizontal magnetic fields. Poloidal convection rolls are, therefore, common, since their flow is aligned and circulates around the magnetic field lines. If the sidewall is cylindrical, boundary conditions further encourage poloidal convection rolls. Such rolls have been observed in liquid metal battery experiments, and the characteristic speed increases as Ha increases [120,121]. Simulations have shown similar results, with the number of convection rolls decreasing as the current increases [122]. Other simulations, however, have suggested that electromagnetic effects are negligible for liquid metal batteries with radius less than 1.3 m [123,124]. Further study may refine our understanding. In batteries with a rectangular cross section, we would expect horizontal convection rolls circulating around cores that are nearly circular near the central axis of the battery, where the magnetic field is strong and the sidewall is remote. Closer to the wall, we would expect rolls circulating around cores that are more nearly rectangular due to boundary influence.

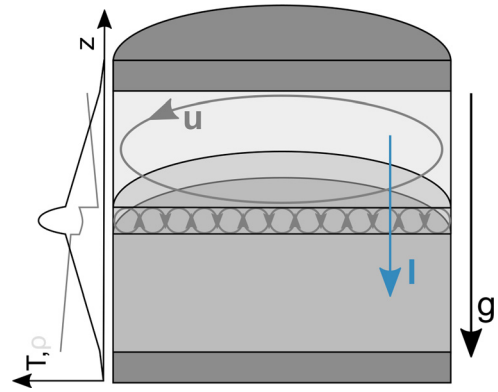

Fig. 7 Sketch of a liquid metal cell with thermal convection

3.5 Convection in Liquid Metal Batteries. Liquid metal batteries as sketched in Fig. 7 are a more complicated and interesting case than a single layer system. Commercially viable liquid metal battery chemistries involve materials that are solid at room temperature; to operate, they must be heated to 475 °C [15]. External heaters produce thermal convection in almost any arrangement, especially the most efficient one in which heaters are installed below the batteries, producing the Rayleigh–Bénard case. During operation, however, external heaters are often unnecessary because the electrical resistance of the battery components converts electrical energy to heat in a process known as Joule heating or ohmic heating. If the battery current is large enough and the environmental heat loss is small enough, batteries can maintain temperature without additional heating [125]. (In fact, cooling may sometimes be necessary.) In this case, the primary heat source lies not below the battery, but within it. As Table 3 shows, molten salts have electrical conductivity typically four orders of magnitude smaller than liquid metals, so that essentially all of the Joule heating occurs in the electrolyte layer, as shown in Fig. 8. The positive electrode, located below the electrolyte, is then heated from above and becomes stably stratified; its thermal profile actually hinders flow. Some flow may be induced by the horizontal motion of the bottom of the electrolyte layer, which slides against the top of the positive electrode and applies viscous shear stresses, but simulations of Boussinesq flow show the effect to be weak [123,124]. The electrolyte itself, which experiences substantial bulk heating during battery charge and discharge, is subject to thermal convection, especially in its upper half [124,131]. One simulation of an internally heated electrolyte layer showed it to be characterized by small, round, descending plumes [132]. Experiments have raised concern that thermal convection could bring intermetallic materials from the electrolyte to contaminate the negative electrode [133]. Convection due to internal heating has also been studied in detail in other contexts [134].

The negative electrode, located above the electrolyte, is heated from below and is subject to thermal convection. In a negative electrode composed of bulk liquid metal, we would expect both unstable thermal stratification and viscous coupling to the adjacent electrolyte to drive flow. Simulations show that in parameter regimes typical of liquid metal batteries, it is viscous coupling that dominates; flow due to heat flux is negligible [123]. Therefore, in the case of a thick electrolyte layer, mixing in the

Table 3 Properties of common electrolyte materials, from Janz et al. [126,127], Todreas et al. [128], Kim et al. [11], and Masset et al. [129,130]

Material	$\nu/10^{-6}$ (m^2/s)	ρ (kg/m^3)	σ_E (S/m)
LiF	1.228	1799	860
LiCl	1.067	1490	586
LiI	0.702	3.0928	396.68
NaCl	0.892	1547	363
$CaCl_2$	1.607	2078	205.9
$BaCl_2$	1.460	3.150	216.4
NaOH	2.14	1767	244
NaI	0.532	2725.8	229.2
$ZnCl_2$	1150	2514	0.268
LiCl–KCl (58.5–41.5) mol %	1.560	1563	157.2
NaCl–KCl–$MgCl_2$ (30–20–50) mol %	0.688	1715	80
LiCl–LiF–LiI (29.1–11.7–59.2) mol %	—	2690	288

electrolyte is stronger than mixing in the negative electrode above; in the case of a thin electrolyte layer, the roles are reversed [123]. However, the negative electrodes may also be held in the pores of a rigid metal foam by capillary forces, which prevents the negative electrode from contacting the battery sidewall [15]. The foam also substantially hinders flow within the negative electrode. Essentially, the characteristic length scale becomes the pore size of the foam, which is much smaller than the thickness of the negative electrode. Since the Rayleigh number is proportional to the cube of the characteristic length scale (Eq. (7)), convection is drastically weakened, if not prevented altogether. The physics of convection in porous media [135,136] might apply in this case.

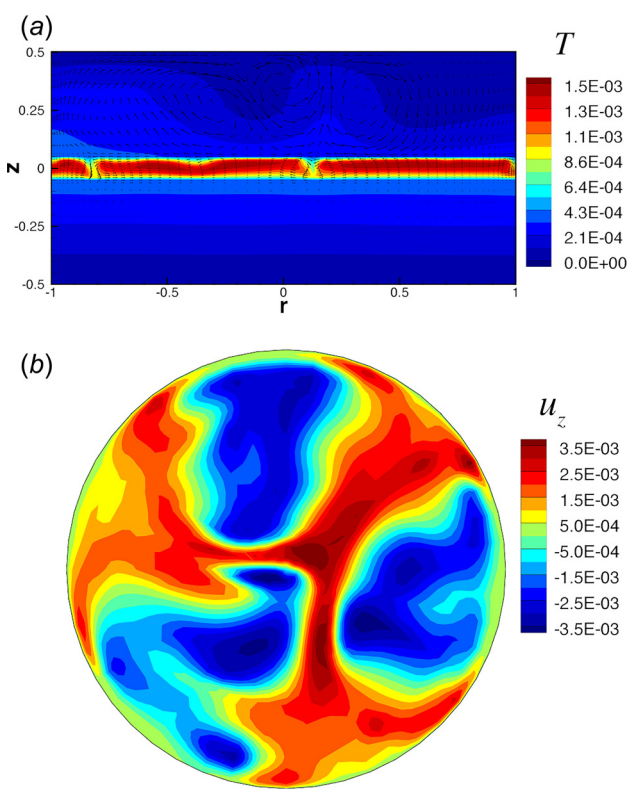

Fig. 8 A simulation of thermal convection in a three-layer liquid metal battery. A vertical cross section through the center of the battery (*a*) shows that the temperature is much higher in the electrolyte than in either electrode. A horizontal cross section above the electrolyte (*b*) shows vigorous flow. Here, u_z is the vertical velocity component, the radius and thickness of the battery are 52 mm, and the LiCl–KCl electrolyte makes up 10% of the thickness. Adapted from Ref. [123], with permission.

If a liquid metal battery is operated with current density that is uniform across horizontal cross section, we expect uniform Joule heating, and therefore, temperatures that vary primarily in the vertical direction (aside from thermal edge effects). However, the negative current collector must not make electrical contact with the vessel sidewall, which is part of the positive current collector. For that reason, the metal foam negative current collector that contains the negative electrode is typically designed to be smaller than the battery cross section, concentrating electrical current near the center and reducing it near the sidewall. The fact that current can exit the positive electrodes through the sidewalls as well as the bottom wall allows further deviation from uniform, axial current. Nonuniform current density causes Joule heating that is also nonuniform—in fact, it varies more sharply, since the rate of heating is proportional to the square of the current density. This gradient provides another source of convection-driven flow. Putting more current density near the central axis of the battery creates more heat there and causes flows that rise along the central axis. Interestingly, electro-vortex flow (considered in detail in Sec. 7) tends to cause the opposite motion: descent along the central axis. Simulations have shown that negative current collector geometry and conductivity substantially affect flow in liquid metal batteries [137]. Other geometric details can also create temperature gradients and drive convection. For example, sharp edges on a current collector concentrate current and cause intense local heating. The resulting local convection rolls are small but can nonetheless alter the global topology of flow and mixing. Also, if solid intermetallic alloys form, they affect the boundary conditions that drive thermal convection. Intermetallics are typically less dense than the surrounding melt, so they float to the interface between the positive electrode and electrolyte. Intermetallics typically have lower thermal and electrical conductivity than the melt, so where they gather, both heating and heat flux are inhibited, changing convection in nontrivial ways.

4 Marangoni Flow

The molecules of a stable fluid are typically attracted more strongly to each other than to other materials. The result is the surface tension (or surface energy) σ, which can be understood as an energy per unit area (or a force per unit length) of interface between two materials. The surface tensions of liquid metals and molten salts are among the highest of any known materials, so it is natural to expect surface tension to play a role in liquid metal batteries. This section will consider that role.

If the surface tension varies spatially, regions of higher surface tension pull fluid along the interface from regions of lower surface tension. Viscosity couples that motion to the interior fluid, causing "Marangoni flow," sketched in Fig. 9. Surface tension can vary spatially because it depends on temperature, chemical composition, and other quantities. For most fluids, surface tension decreases with temperature: $\partial\sigma/\partial T < 0$, and flow driven by the variation of surface tension with temperature is called "thermocapillary flow" and is described in existing reviews [138–140]. Thermocapillary flow in the presence of a magnetic field has also been studied in prior work [141,142], though we will not consider it further here. Flow driven by the variation of surface tension with composition, called "solutal Marangoni flow," has also been considered [143–146], especially in the context of thin films [146,147]. In this section, we will consider Marangoni flow phenomena that are relevant to liquid metal batteries, focusing on similarities and differences to Marangoni flows studied in the past. We will estimate which phenomena are likely to arise, drawing insight from one pioneering study that has considered the role of thermocapillary flow in liquid metal batteries [131].

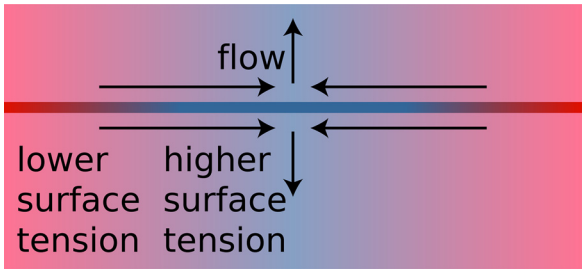

Fig. 9 Marangoni flow occurs when surface tension at a fluid interface varies spatially. Variation along the interface always drives flow, as shown. Variation across the interface, however, causes an instability that drives flow only if the variation is sufficiently large, as quantified by the Marangoni number Ma.

4.1 Introduction to Thermocapillary Marangoni Flow. Thermocapillary flow is driven by temperature gradients but hindered by viscosity, thermal diffusion, and density (which provides inertia). Thermocapillary flow also occurs more readily in thicker fluid layers. Combining these physical parameters produces the dimensionless Marangoni number

$$\mathrm{Ma} = \frac{\left|\frac{\partial \sigma}{\partial T}\right| L \Delta T}{\rho \nu \kappa} \tag{9}$$

The Marangoni number plays a role analogous to the Rayleigh number in thermal convection. Larger values of *Ma* make thermocapillary flow more likely and more vigorous. Because temperature gradients drive both thermocapillary flow and thermal convection, the two phenomena often occur simultaneously. We can compare their relative magnitudes via the dynamic Bond number

$$\mathrm{Bo} = \frac{\mathrm{Ra}}{\mathrm{Ma}} = \frac{\rho \alpha_T g L^2}{\left|\frac{\partial \sigma}{\partial T}\right|} \tag{10}$$

Thermal convection dominates when $\mathrm{Bo} \gg 1$, whereas thermocapillary flow dominates when $\mathrm{Bo} \ll 1$. Because of the L^2 factor, thermal convection tends to dominate in thick layers, whereas thermocapillary flow tends to dominate in thin layers. Thermocapillary flow, like thermal convection, is qualitatively different for fluids with small Prandtl number (like liquid metals and molten salts) than for fluids with large Prandtl number.

4.2 Temperature Variation Across the Interface. Thermocapillary flow phenomena depend on the direction of the thermal gradient with respect to the interface. Surface tension varying along the interface always drives flow, as shown in Fig. 9. We will consider this case in greater detail later. However, thermocapillary flow can also occur if temperature varies *across* the interface, with the hotter material having smaller thermal diffusivity. In that case, an instability is possible: local perturbations can either change the temperature profile along the interface directly or indirectly through a change to the interface shape, resulting in Marangoni flow. The instability can produce either of two different phenomena, short-wavelength and long-wavelength thermocapillary flow, in which deformations are damped primarily by gravity or diffusion, respectively. The relative strength of the two damping mechanisms is quantified by the Galileo number

$$G = \frac{g d^3}{\nu \kappa} \tag{11}$$

$G \gg 1$ implies that gravity is the primary damping mechanism, such that we expect short-wavelength flow, whereas $G \ll 1$ implies that diffusion of heat and momentum is the primary damping mechanism, such that we expect long-wavelength flow [140,148]. (Note that some past authors [138,139] have used the term "Marangoni flow" for the specific case of thermocapillary flow driven by temperature variation across the interface, not for the much more general case of all flows driven by surface tension, as we use it here.)

In the $G \gg 1$ case, linear stability theory shows that conductive heat transfer becomes unstable and short-wavelength flow arises when $\mathrm{Ma} > 80$ [149], as experimental studies have confirmed [148]. Typically, short-wavelength flow appears as an array of hexagons covering the interface. For $G \leq 120$, linear stability theory predicts that when $\mathrm{Ma} > 2G/3$, instead of short-wavelength flow, long-wavelength flow arises [148,150]. The long-wavelength flow has no repeatable or particular shape, instead depending sensitively on boundary conditions. When observed in experiments, the long-wavelength flow always ruptures the layer in which it occurs [139], a property particularly alarming for designers of liquid metal batteries. The short-wavelength mode, on the other hand, causes nearly zero surface deformation [139].

We can estimate the relevance of thermocapillary flow and the likelihood of short-wavelength and long-wavelength flow using dimensionless quantities, as long as the necessary material properties are well-characterized. Most difficult to obtain is the rate of change of surface tension with temperature, $\partial\sigma/\partial T$. Its value is well-known for Pb, Bi, and their eutectic alloy [102] because of its importance in nuclear power plants, however. One pioneering study [131] simulated thermocapillary flow in a hypothetical three-layer liquid metal battery with a eutectic PbBi positive electrode, a LiCl–KCl electrolyte, and a Li negative electrode. First considering the positive electrode, for a PbBi layer with $L = 20$ mm and $\Delta T = 0.5$ K (the conditions used in the study), we expect no short-wavelength flow because, according to Eq. (9), $\mathrm{Ma} = 14 < 80$. Nor do we expect long-wavelength flow because, according to Eq. (11), $G = 6 \times 10^7 \gg 120$. Now considering a LiCl–KCl electrolyte layer with $L = 20$ mm and $\Delta T = 6$ K (again matching [131]), we come to different conclusions: $\mathrm{Ma} = 23{,}000$ implies vigorous thermocapillary flow, and $\mathrm{Bo} = 9$ leads us to expect thermocapillary flow of speed similar to the thermal convection. Because $G = 4.7 \times 10^6$, we expect the short-wavelength mode, not the long-wavelength mode. Finally, we expect minimal flow in the negative electrode if it is contained in a rigid metal foam. All of these predictions should be understood as preliminary since Eqs. (9)–(11) consider a layer in which only one surface is subject to surface tension effects, but the electrolyte layer in a liquid metal battery is subject to surface tension effects on both upper and lower surfaces.

In fact, though the long-wavelength mode can readily be observed in laboratory experiments with silicone oils [148,151,152], liquid metals and molten salts typically have much smaller kinematic viscosity and thermal diffusivity, yielding large values of G that make the long-wavelength mode unlikely. Using the $\mathrm{Ma} > 2G/3$ criterion and the appropriate material properties, we find that the long-wavelength mode will appear only for thicknesses 60 μm or less in either the PbBi or LiCl–KCl layer. Other considerations require both the electrolyte and the positive electrode to be much thicker, so rupture via the long-wavelength thermocapillary mode is unlikely in a liquid metal battery.

We would expect, however, that the short-wavelength thermocapillary mode often arises in liquid metal batteries, especially in the electrolyte layer. Though unlikely to rupture the electrolyte, the short-wavelength mode may mix the electrolyte, promoting mass transport. The short-wavelength mode might also couple to other phenomena, for example, the interfacial instabilities discussed in Sec. 5.

4.3 Temperature Variation Along the Interface. Temperature that varies along the interface always drives Marangoni flow, and we can estimate its speed by considering the energy involved.

Suppose a thin, rectangular layer of fluid occupies the region $0 \le x \le L_x$, $0 \le y \le L_y$, $0 \le z \le L_z$ in Cartesian coordinates (x, y, z), with $L_z \ll L_x$ and $L_z \ll L_y$. Suppose thermocapillary forces act on the $z = L_z$ surface, and that temperature varies in the x direction, such that surface tension drives flow in the x direction. The work done by thermocapillary forces (per unit volume) scales as

$$\frac{\Delta T \dfrac{\partial \sigma}{\partial T} L_x L_y}{L_x L_y L_z}$$

If the flow is steady, if pressure variations are negligible, and if inertial and gravitational forces are negligible, then the work done by thermocapillary forces must be dissipated by viscous damping. For an incompressible Newtonian fluid, the viscous damping term (in energy per unit volume) reads

$$\mu \tau u_j \left(\frac{\partial^2 u_i}{\partial x_i \partial x_j} + \frac{\partial^2 u_j}{\partial x_i \partial x_j} \right)$$

where we use indicial notation with summation implied, u_j is a velocity component, and τ is a characteristic flow time. We can estimate the flow time in terms of a characteristic speed U and the total circulation distance $\tau \sim (L_x + L_z)/U$. If there is no flow in the y direction and no flow variation in the x direction, we can estimate the gradients in the viscous damping term as well. Setting the result equal to the work (per unit volume) done by capillary forces and solving for U, we estimate a characteristic speed

$$U \sim \frac{\Delta T \dfrac{\partial \sigma}{\partial T}}{\mu} \frac{L_z}{L_z + L_x}$$

As expected, the speed increases with ΔT and $\partial\sigma/\partial T$, which increases the thermocapillary force; and increases with L_z, which reduces viscous shear; but decreases with μ, L_z, and L_x, which increases viscous drag. Again considering the model of [131], we find $U \sim 0.4$ mm/s in the PbBi positive electrode and $U \sim 8$ mm/s in the LiCl–KCl electrolyte. Figure 19 in Ref. [131] shows velocities around 2 mm/s, so our velocity scaling argument seems to predict the correct order of magnitude.

Simulations can give further insight into thermocapillary flow in liquid metal batteries. Köllner et al. [131] considered a model liquid metal battery with uniform current density that caused Joule heating in all three layers, thereby causing both thermocapillary flow and buoyancy-driven thermal convection. As shown in Fig. 10, Marangoni cells are evident at the top of the electrolyte, and the temperature is much higher in the electrolyte than in either electrode, consistent with Fig. 8. Using a range of layer thicknesses and current densities, the study found that five modes of thermal flow arise in typical liquid metal batteries. In order of decreasing typical speed, they are (1) thermal convection in the electrolyte, (2) thermal convection in the negative electrode, (3) thermocapillary flow driven by the top surface of the electrolyte, (4) thermocapillary flow driven by the bottom surface of the electrolyte, and (5) anticonvection [153] in the positive electrode. The combined effects of buoyant and thermocapillary forces produce flows much like those produced by buoyancy alone, though thermocapillary forces slightly reduce the characteristic length scale of the flow. That observation is consistent with an earlier observation that thermocapillary and buoyant forces drive flows having different characteristic lengths [151]. In the electrolyte, thermocapillary forces always augment buoyant flow, but in the negative electrode, thermocapillary forces oppose and substantially damp buoyant flow when $\mathrm{Ma} < 200$ [131]. Electrolyte layers thinner than 2 mm exhibit neither thermocapillary flow nor thermal convection for realistic current densities (less than 2000 A/m^2). We raise one caveat: if the negative electrode is contained by a metal foam, flow there would likely be negligible.

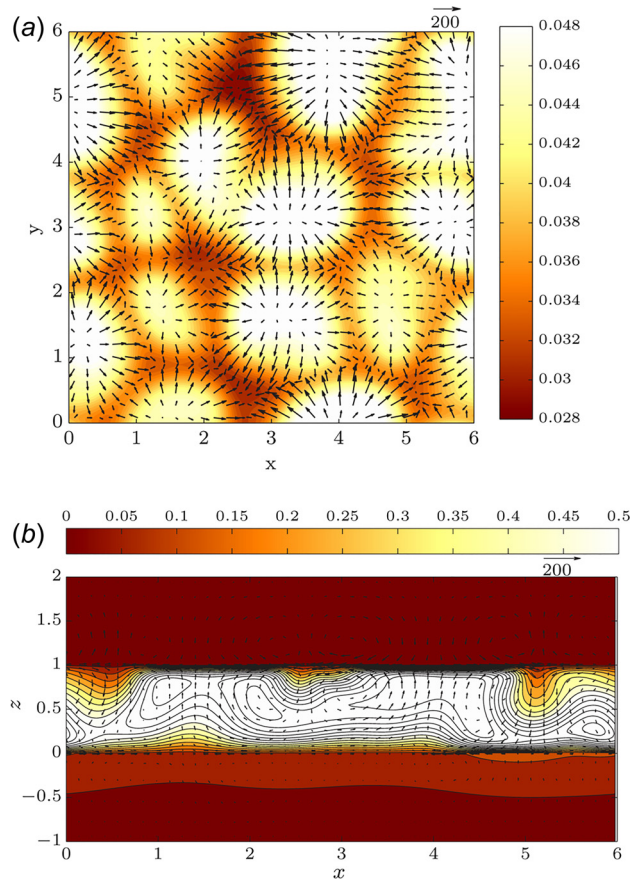

Fig. 10 A simulation of Marangoni flow in a three-layer liquid metal battery. Temperature is indicated in color, and velocity is indicated by arrows. The horizontal top surface of the electrolyte shows Marangoni cells (*a*) with downwellings where the temperature is lowest. A vertical cross section through the center of the battery, (*b*) also shows downwellings and indicates that the temperature is much higher in the electrolyte than in either electrode. Here, a LiCl–KCl electrolyte separates a Li negative electrode from a PbBi positive electrode. The temperature unit is 6.59 K, the velocity unit is 6.46×10^{-6} m/s, and the length unit is 20 mm. Adapted from Ref. [131], with permission.

4.4 Introduction to Solutal Marangoni Flow. Solutal Marangoni flow has been studied less than thermocapillary flow, and to our knowledge, has not yet been addressed in the literature for the specific case of liquid metal batteries. One experimental and numerical study found a cellular flow structure reminiscent of the hexagons characteristic of the short-wavelength mode in thermocapillary flow [144]. A later experimental and numerical study by the same authors [145] varied the thickness of the fluid layer and its orientation with respect to gravity, finding that a two-dimensional simulation in which flow quantities are averaged across the layer thickness fails to match experiments with thick layers. The study also found that cells coarsen over time, perhaps scaling as $t^{1/2}$, where t is the time.

Though studies of solutal Marangoni flow in liquid metal batteries have not yet been published, the phenomenon is likely, because charge and discharge alter the composition of the positive electrode. In past work, salt loss in lithium-chalcogen cells has been attributed to Marangoni flow [154]. In the case where composition varies across the interface, solutal Marangoni flow is possible only if material flows across the interface in the direction of increasing material diffusivity. In a liquid metal battery, the material of interest is the negative electrode material, e.g., Li, and the interface of interest is the one between molten salt electrolyte and liquid metal positive electrode. The diffusivity of Li in Bi is

1.2×10^{-8} m^2/s, and the diffusivity of Li in LiBr–KBr has been calculated as 2.4×10^{-9} m^2/s [155]. A battery made with those materials would be prone to solutal Marangoni flow driven by composition varying across the interface during discharge, but not during charge. Solutal Marangoni flow driven by variations across the interface is likely to occur in both short- and long-wavelength modes, depending on the appropriate Marangoni and Galileo numbers (analogous to Eqs. (9) and (11)). However, a two-layer model for solutal Marangoni flow is unstable at any value of the Marangoni number [138,156]. Variations of composition along the interface will drive solutal Marangoni flow regardless of their values.

An estimate of the magnitude of solutal Marangoni flow would be useful. Even less is known about the rate of change of surface tension with composition than about the rate of change with temperature. Still, we can put an upper bound on the magnitude of solutal Marangoni flow, and compare to thermocapillary flow, by considering extreme cases. The force per unit length that drives thermocapillary flow is

$$\left|\frac{\partial \sigma}{\partial T}\Delta T\right|$$

Again considering the same situation as [131], we find a force per unit length around 1.8×10^{-4} N/m. The force per unit length that drives solutal Marangoni flow is

$$\left|\frac{\partial \sigma}{\partial X}\Delta X\right|$$

Unfortunately, $\partial\sigma/\partial X$ is, to our knowledge, unknown in the literature for materials common to liquid metal batteries. Alternatively, we can consider the extreme case in which different regions of the interface are composed of different pure materials, so that the force per unit length is simply the difference between their (known) surface tensions. Using $\sigma_{PbBi} = 0.4086$ N/m at 500 K [102], $\sigma_{Li} = 0.396$ N/m at 453 K [105], and $\sigma_{LiCl\text{–}KCl} = 0.122$ N/m at 823 K [157], we find $\sigma_{PbBi} - \sigma_{Li} = 1.3 \times 10^{-2}$ N/m and $\sigma_{Li} - \sigma_{LiCl\text{–}KCl} = 2.7 \times 10^{-1}$ N/m. These estimates are imprecise: considering temperature will change them by a few percent, and considering different battery chemistry will change them more. These estimates are also upper bounds. Nonetheless, these estimates are two to four orders of magnitude larger than the typical force per unit length that drives thermocapillary flow. If the true solutal forces reach even a few percent of these estimates, solutal Marangoni flow rivals or dominates thermocapillary flow in liquid metal batteries. Better constraints on the magnitude of solutal Marangoni flow—beginning with estimates of $\partial\sigma/\partial X$—would be a valuable contribution for future work.

5 Interface Instabilities

It is a well-known phenomenon in Hall–Héroult, i.e., AECs, that long wave instabilities can develop at the interface of the cryolite and the liquid aluminum [158–161]. Those instabilities are known as "sloshing" or "metal pad roll instability." Not only because AECs gave the inspiration for the initial LMB concept at MIT [88] it is worthwhile to have a closer look at the role of interface instabilities in LMBs. If the interface between a good electric conductor (metal, $\sigma = O(10^6)$ S/m) and a poor one (electrolyte, $\sigma_{el} = O(10^2)$ S/m) is slightly inclined with respect to the horizontal plane, the current distribution inside the layers changes. In the metal layer(s), horizontal perturbation currents (I_h) arise as sketched in Fig. 11. Those horizontal currents interact with the vertical component of a background magnetic field generated, e.g., by the current supply lines, generating Lorentz forces that set the metal layer into motion. This mechanism was first explained by Sele [158] for AECs. As a consequence, gravity waves with a characteristic length of the vertical cell size develop and culminate in a sloshing motion of the aluminum. Wave amplitudes may become large enough to reach the graphite negative electrodes

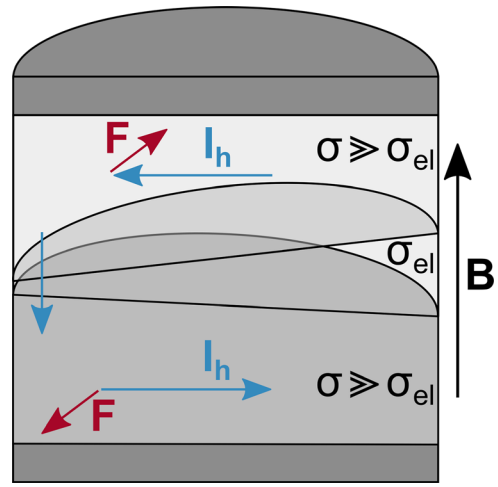

Fig. 11 Sketch of a liquid metal cell undergoing an interfacial instability

and short-circuit the cell, thereby terminating the reduction process. In order to prevent the waves from contacting the negative electrodes for a cell current of about 350 kA, considered as an upper limit for modern cells [162], a cryolite layer at least 4.5 cm thick is required [159]. These boundary conditions mean that nearly half of the cell voltage is spent overcoming the electrolyte resistance, and the corresponding electric energy is converted to heat [159]. Reducing the electrolyte layer thickness by even a few millimeters would result in large cost savings, but is made impossible by the sloshing instabilities. Admittedly, Joule heating is not entirely wasted, because it maintains the high cell temperature and permits the strong wall cooling that allows the formation of the side-wall protecting ledge [160]. Metal pad rolling in AECs, which typically have a rectangular cross section, occurs if the parameter

$$\beta = \frac{JB_z}{g\Delta\rho_{CE}} \cdot \frac{L_x}{H_E} \cdot \frac{L_y}{H_C} \tag{12}$$

exceeds a critical value β_{cr}. Here J and B_z denote the absolute values of the cell's current density and of the vertical component of the background magnetic field, respectively, $\Delta\rho_{CE}$ is the density difference between cryolite and aluminum, and H_E, H_C and L_x, L_y refer to the layer heights and the lateral dimensions of the AEC, respectively. See Fig. 12 (left) for reference. The first factor in Eq. (12) is the ratio of Lorentz force to gravity force, and the latter ones are ratios of layer height to lateral cell dimension.

Bojarevičs and Romerio [163] obtained an expression for β_{cr} depending on wave numbers of gravity waves m, n in the x, y directions developing in rectangular cells

$$\beta_{cr} = \pi^2\left|m^2\frac{L_y}{L_x} - n^2\frac{L_x}{L_y}\right| \tag{13}$$

According to Eq. (13), cells with square or circular cross section are always unstable because their lateral dimensions are equal and thus $\beta_{cr} = 0$. Davidson and Lindsay [164] came to a similar conclusion regarding the instability threshold for circular and square cells using both shallow water theory and a mechanical analog.

It can be expected that three-layer systems like Al refinement cells (cf. Sec. 2.1) and LMBs will exhibit features similar to those found in AECs, but the addition of the second electrolyte-metal interface should enrich system dynamics. Knowledge on three-layer systems bearing interface normal currents is currently relatively scarce. Sneyd [165] treated the case while modeling an

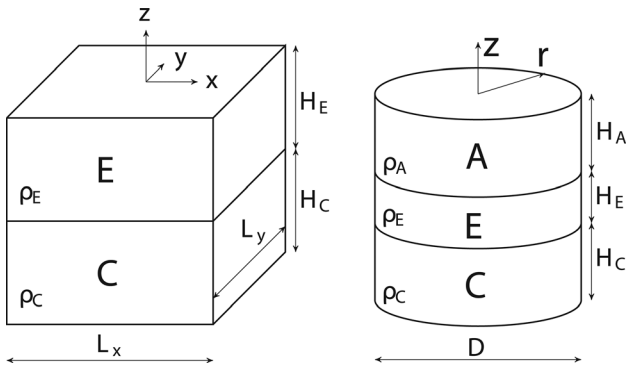

Fig. 12 Characteristic dimensions and notations for an aluminum electrolysis cell (left) and a liquid metal battery (right)

electric-arc furnace, assuming a density of zero for the upper phase and the semi-infinite upper and lower layers. He took only the azimuthal magnetic field produced by the current into account and did not consider the action of an additional background field. In addition to long-wave instabilities, Sneyd predicted short-wave instabilities of both sausage and kink type. To the best of our knowledge, experimental results on current-driven interface instabilities in three-layer systems have not been reported to date. The cause of the violent motions reported by several authors [28,38,32,42], and already mentioned in Sec. 2.1, is uncertain. Frary [28] describes the motion as swirling and attributes it to the interaction of the vertical current within the cell and the magnetic fields of the horizontal current leads. To prevent intermixing of the negative and positive electrodes, the electrolyte layer has to be as thick as 25 cm. This is costly in terms of energy but tolerable if the cell is operated as an electrolytic cell. In galvanic mode, OCV obviously limits the permissible current and the resistance of thick electrolyte layers is prohibitive. For LMBs to have an acceptable voltage efficiency, the electrolyte thickness must not exceed a few millimeters, so maintaining interface stability is more difficult.

Zikanov [166] was the first to discuss sloshing behavior in three-layer systems explicitly addressing LMBs. He used a mechanical analog inspired by Davidson and Lindsay's [164] movable aluminum plate model for the basic features of sloshing in AECs. Instead of one plate mimicking the aluminum layer of an AEC, Zikanov assumed two slabs of solid metals to be suspended as pendula above and below the electrolyte layer [124]. This model replaces the hydrodynamic problem by a system possessing only four degrees-of-freedom associated with the two-dimensional oscillations of each pendulum. The Lorentz force due to the interaction of the vertical background magnetic field and the horizontal currents can cause an instability if

$$C_A \frac{JB_z L_x^2}{12 g \rho_A H_E H_A} + C_C \frac{JB_z L_x^2}{12 g \rho_C H_E H_C} > \left| 1 - \frac{\omega_x^2}{\omega_y^2} \right| \tag{14}$$

Here C_A and C_C are constants of order one that account for geometry [166], and ρ_A and ρ_C denote the densities of the negative and positive electrodes, respectively. The pendula oscillate with their natural gravitational frequencies ω_x and ω_y. Again, it is evident from Eq. (14) that circular or square cross sections are predicted to be always unstable.

Zikanov [166] and Zikanov and Shen [124] discussed an additional instability that may arise even in the absence of a background magnetic field due to the interaction of J-generated azimuthal magnetic field B_φ with the current perturbations. He finds the system to be unstable if

$$\frac{\mu_0 J^2 D^2}{64 g} \left(\frac{D^2}{12 \rho_A H_A H_E^2} + \frac{D^2}{12 \rho_C H_C H_E^2} + \frac{1}{\rho_A H_E} - \frac{1}{\rho_C H_E} \right) > 1 \tag{15}$$

As estimated by Zikanov [166], for rectangular cells, the instability due to the interaction of the perturbation currents with the azimuthal field of the main current described by criterion (15) appears to be more dangerous than that caused by the action of the background magnetic field on the horizontal compensating currents (14).

It should be mentioned that criteria predicting instability onset for any nonvanishing Lorentz force neglect dissipative effects caused by magnetic induction and viscosity as well as the influence of surface tension [167].

Weber et al. [167,168] investigated the metal pad roll instability in an LMB using a volume-of-fluid method adapted from the finite volume code OpenFOAM [169] and supplemented by electromagnetic field calculations to solve the full Navier–Stokes equations. The material properties correspond to the special case of the Mg|KCl–$MgCl_2$–NaCl|Sb system (see Table 4 for an overview of typical systems).

As expected, if one interface is set in motion and the other remains nearly at rest, a criterion similar to the Sele criterion (12) can be formulated

$$\beta = \frac{JB_z D^2}{g(\rho_E - \rho_A) H_A H_E} > \beta_{cr} \tag{16}$$

using the density differences between negative electrode and electrolyte and the respective layer heights. Sloshing in circular cells sets in above a relatively well-defined $\beta_{cr,sloshing} = 0.44$. Short-circuiting needs more intense Lorentz forces and happens above $\beta_{cr,short\text{-}circuit} \approx 2.5$. The validity of both values is limited to the Mg||Sb system and to the aspect ratios $H_A/D = 0.45$ and $H_E/D = 0.1$ investigated by Weber et al. [167], see Fig. 13.

Bojarevics and coworkers [96,97] numerically investigated the Mg||Sb system as well, but used a shallow water approximation combined with the electromagnetic field equations. They considered a cell with a $8 \times 3.6\ m^2$ cross section, and Mg and Sb layers both 20 cm in height divided by a 5 or 8 cm thick electrolyte. In

Table 4 Coupling parameter $\mathcal{A}_g$ calculated for different possible working material combinations. The densities are reported at working temperature T_{op}, adapted from Ref. [170].

	Electrodes	Electrolyte	T_{op} (°C)	ρ_A	ρ_E (kg m^{-3})	ρ_C	$\mathcal{A}_g$
Strongly coupled	Li||Se	LiCl–LiF–LiI	375	497	2690	3814	0.51
	Al||Al–Cu*	AlF_3–NaF–$CaCl_2$–NaCl	800	2300	2700	3140	1.1
	Li||Te	LiCl–LiF–LiI	475	489	2690	5782	1.41
Weakly coupled	Na||Sn	NaCl–NaI	625	801	2420	6740	2.67
	Li||Bi	LiCl–LiF–LiI	485	488	2690	9800	3.22
	Na||Bi	NaCl–NaI–NaF	550	831	2549	9720	4.18
	K||Hg	KBr–KI–KOH	250	640	2400	12,992	6.02
Not coupled	Ca||Sb	$CaCl_2$–LiCl	700	1401	1742	6270	13.28
	Ca||Bi	$CaCl_2$–LiCl	550	1434	1803	9720	21.43
	Mg||Sb	KCl–$MgCl_2$–NaCl	700	1577	1715	6270	33.06

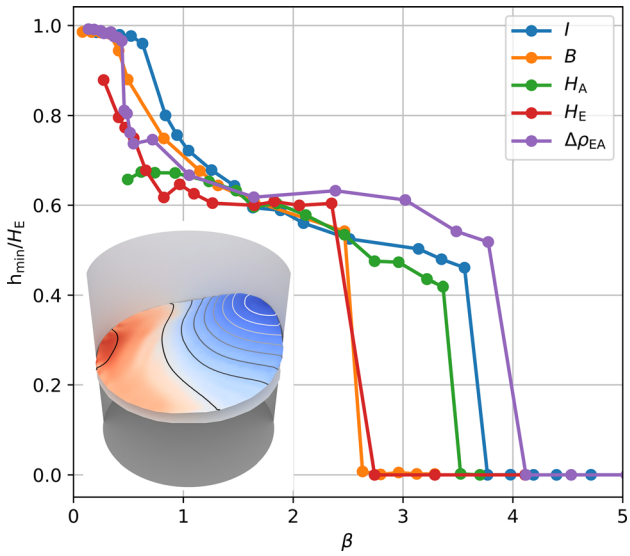

Fig. 13 Minimum electrolyte layer height h_{min} depending on β according to Eq. (16) for the Mg|KCl–$MgCl_2$–NaCl|Sb system, determined in simulations. For each curve, only the parameter named in the legend is varied, the other ones stay constant ($j = 1$ A/cm^2, $B_z = 10$ mT, $H_A = 4.5$ cm, $H_E = 1$ cm, and $\rho_A = 1577$ kg/m^3). By definition, $\Delta\rho_{EA} = \rho_E - \rho_A$. The inset shows a snapshot of the anode-electrolyte interface for $\beta = 2.5$. Adapted from Ref. [167].

agreement with the results of Weber et al. [167,168], Bojarevics and coworkers [96,97] found the interface between negative electrode and electrolyte to be much more sensitive to the instability than the interface between the electrolyte and positive electrode. The difference is explained by density differentials: the electrolyte typically has density closer to that of the negative electrode than the positive electrode. Bojarevics and Tucs [97] further optimized the magnetic field distribution around the LMB by reusing a commercial Trimet 180 kA cell series in their simulation. While the unoptimized cell could only be stabilized for the 8 cm thick electrolyte, the optimized cell was able to operate with 2.5 cm electrolyte height. However, even in the latter case, the voltage drop in the electrolyte is still found to be excessive with 0.49 V at a current of 100 kA.

Horstmann et al. [170] investigated the wave coupling dynamics of both interfaces by applying potential theory as well as direct numerical simulations to LMBs with circular cross section. While interface tension should be taken into account for (very) small cells and large wave numbers, it is negligible in the limit of large-scale LMBs. There, the waves are purely gravitational ones and the strength of their coupling depends only on the ratio of the density differences

$$\mathcal{A}_g = \frac{\rho_C - \rho_E}{\rho_E - \rho_A} \tag{17}$$

Thus, for practical cases, $\mathcal{A}_g$ is the control parameter that determines how strongly both interfaces interact. Wave onset is described by Sele-like parameters extended by interface tension terms for both interfaces. The expressions reduce to the Sele criterion (16) in the limit of large LMBs considered here.

At the same time, $\mathcal{A}_g$ describes for thin electrolyte layers ($H_E \to 0$) the ratios of amplitudes and frequencies of the (antiphase) waves

$$\left|\frac{\hat{\eta}_{AE}^{mn}}{\hat{\eta}_{EC}^{mn}}\right| = \frac{\omega_{EC}^2}{\omega_{AE}^2} = \mathcal{A}_g \tag{18}$$

Here $\hat{\eta}_{AE}^{mn}$ and $\hat{\eta}_{EC}^{mn}$ denote the amplitudes of the of the waves at the AE and EC interfaces, respectively, with the azimuthal wave number m and the radial wave number n. ω_{AE} and ω_{EC} are the corresponding frequencies.

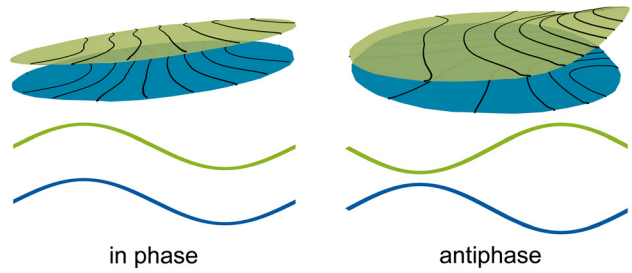

Fig. 14 In phase and antiphase sloshing waves. Simulated interface shapes (top) and idealized circumferential wave contours (bottom). Adapted from Ref. [170].

The waves at both interfaces can be considered as coupled in the range $0.1 < \mathcal{A}_g < 10$. If the metal layer with density more similar to the electrolyte is thinner, the limiting values have to be corrected by the metal layer height ratio H_C/H_A. The coupled regime can be further divided into "weakly coupled" ($0.1 < \mathcal{A}_g \lesssim 0.7$, $2 \lesssim \mathcal{A}_g < 10$) and "strongly coupled" ($0.7 \lesssim \mathcal{A}_g \lesssim 2$) regimes. The threshold values are empirical. In the weakly coupled regime, the interface waves are antiphase (see Fig. 14) and corotate in the direction determined by the more prominent wave. Dynamics in the strongly coupled regime are more complex. For moderate $\beta \approx 1.6$, both metals rotate in opposite directions deforming the electrolyte layer into a bulge ("bulge instability"). Higher β (≈ 3.2) leads to in phase rotating metal pads ("synchronous tilting instability"). These strongly coupled instabilities may not occur in cells that are not circular, however. Note that β should be calculated with the densities and length scales corresponding to the smaller density jump. This happened always at the upper interface for the examples discussed earlier. Thus, Eq. (16) could directly be applied.

While the two strongly coupled LMB types (Li||Te and Li||Se) have limited practical relevance due to the scarcity of their positive electrode materials, three-layer refinement cells are almost always strongly coupled. Gesing et al. [45,46] formulate it as a characteristic of their Mg-electrorefinement method that the electrolyte has to have a density halfway between that of Al and Mg, i.e., they require a coupling parameter $\mathcal{A}_g = 1$.

Zikanov [171] used the St. Venant shallow water equations complemented by electromagnetic force terms to model the rolling pad instability in LMBs with rectangular cross sections. In accordance with Horstmann et al. [170], Zikanov [171] found that the wave dynamics depend on the ratio of the density jumps at both interfaces. If the density jump at one interface is much smaller than at the other, only the former develops waves, and the situation is very similar to that in AECs. In particular, the influence of the horizontal aspect ratio L_x/L_y on the critical value of the Sele criterion is quite strong and resembles the situation in AECs. This strong effect can be explained by the fact that the aspect ratio determines the set of available natural gravitational wave modes and the strength of the electromagnetic field that is needed to transform them into a pair with complex-conjugate eigenvalues [164,171].

For comparable density jumps at the interfaces, Zikanov's [171] results again agree with those of Horstmann et al. [170] in that both interfaces are significantly deformed. The system behavior becomes more complex and is different from that found in AECs. The waves of both interfaces can couple either in phase or antiphase. Zikanov [171] found examples where the presence of the second interface stabilizes the system, which was not predicted by his two-slab model [166], whose simplifications are probably too strong to capture this part of the dynamics.

6 Tayler Instability

Electric currents induce magnetic fields and interact with those fields, sometimes bringing unexpected consequences. Suppose

that a current runs axially and has azimuthally symmetric current density $\boldsymbol{J}$, as sketched in Fig. 15. Then, by the right-hand rule, it induces a magnetic field $\boldsymbol{B}_\varphi$ that is purely in the azimuthal direction and interacts with that field to cause a Lorentz force per unit volume $\boldsymbol{F}_L = \boldsymbol{J} \times \boldsymbol{B}_\varphi$ directed radially inward. That force can be understood as a magnetic pressure. If the current flows through a fluid that is incompressible, we might expect the magnetic pressure to have no effect. However, Tayler [172,173] and Vandakurov [174] showed that if the fluid is inviscid ($\nu = 0$) and a perfect conductor ($\sigma_E = \infty$), and the induced magnetic field satisfies

$$\frac{\partial}{\partial r}\left(rB_\varphi^2\right) < 0 \tag{19}$$

then the stagnant system is unstable. Given an infinitesimal perturbation, the current drives fluid flow, initially with azimuthal wave number $m = 1$. That phenomenon, known as the Tayler instability in astrophysics and as the kink instability in plasma physics, must also be considered for liquid metal batteries, which supports large axial currents.

In stars, the Tayler instability can in theory overcome gravitational stratification to drive dynamo action, and has therefore been proposed as a source of stellar magnetic fields [175]. In fusion plasma devices, the kink instability [176] can disrupt the magnetic fields that prevent plasma from escaping and must therefore be avoided. First encountered in z-pinch experiments in the 1950s, the kink instability has been studied extensively and reviewed in the plasma physics literature (e.g., Ref. [177]).

Soon after liquid metal batteries were proposed for grid-scale storage, Stefani et al. [178] observed that the technology would be susceptible to the Tayler instability, and that if the resulting flow were strong enough, it could cause rupture the electrolyte layer, destroying the battery. Their observation prompted a series of studies considering methods to avoid the Tayler instability in liquid metal batteries and the likelihood of it causing rupture.

The Tayler instability can be avoided or damped using a variety of techniques. First, in a real fluid with nonzero viscosity and imperfect electrical conductivity, the onset criterion given by Eq. (19) is no longer strictly correct, because viscosity and resistance damp the instability, so that it occurs only if the total current (or Hartmann number) exceeds a nonzero critical value. Second, the instability can be avoided by cleverly routing the battery current to prevent the condition expressed by Eq. (19). Instead of building a cylindrical liquid metal battery carrying an axial current, one can build a battery that is a cylindrical annulus, with an empty central bore. Carrying no current, the bore does not contribute to the induced magnetic field $\boldsymbol{B}_\varphi$, so that a larger current is required before onset [178]. Even better is to route the battery current back through the bore in the *opposite* direction, which prevents the Tayler instability altogether, since Eq. (19) is never satisfied [178,179].

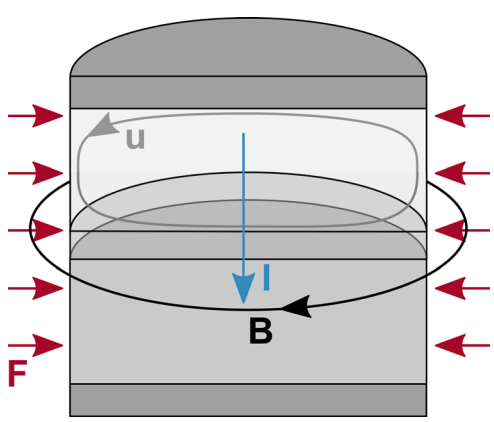

Fig. 15 Sketch of a liquid metal cell susceptible to the Tayler instability

However, ohmic losses in the wire would reduce the available voltage. Third, shearing the fluid azimuthally can damp the Tayler instability [180], though imposing shear is more practical in plasma devices than in liquid metal batteries. Fourth, imposing external magnetic fields—either axial or transverse—damps the Tayler instability [179], in a process often compared to the damping of thermal convection by vertical magnetic fields [112,114]. Finally, rotation also damps the Tayler instability [181], though imposing rotation may be impractical for liquid metal batteries.

A variety of engineering solutions to avoid or damp the Tayler instability in liquid metal batteries are now known. The characteristics of the Tayler instability, and the particular situations in which it arises, have also been studied extensively in recent work. The instability was observed directly in a laboratory experiment: when the axial current applied to a cylindrical volume of GaInSn alloy exceeded a critical value, the induced axial magnetic field was observed to grow as the square root of the current [182]. Below the critical current, which nearly matched earlier numerical predictions [183], no axial field was induced. A central bore was added to the vessel, and as expected, the critical current grew with bore size, ranging from about 2500 A to about 6000 A. Flow due to the Tayler instability was found to compete with thermal convection caused by Joule heating (see Sec. 3).

A series of numerical studies have also considered the Tayler instability, with the benefit of being able to characterize its properties in detail. Initial simulations with purely axial current and perfectly conducting boundaries found the Tayler instability to occur at $\mathrm{Ha} \sim 20$ [181,184,185]. (The Hartmann number (see Eq. (8)) is known to control onset [183].) Using parameters similar to experiments [182], the simulations found similar critical currents. The simulations also demonstrated the importance of aspect ratio: liquid metal layers with high aspect ratio (narrow and tall) are more susceptible to the Tayler instability [185], see Fig. 16. Simulations have also shown the effectiveness of engineering solutions for avoiding or damping the Tayler instability, including adding a central bore, routing current through the bore in the opposite direction, and applying axial or transverse magnetic fields [179]. The Tayler instability breaks chiral symmetry during its growth [184] and might therefore provide a link between the planetary tides and the solar cycle [186]. By allowing for current that is not purely axial, and boundaries that are not perfect conductors, a later simulation [137] incorporated more realistic current collectors and considered their effects. Current collectors with lower conductivity damp the Tayler instability, as do fluids with lower conductivity [137]. That study also found, however, that electro-vortex flows (see Sec. 7) may play a larger role in the fluid mechanics of liquid metal batteries than the Tayler instability. A numerical linear stability analysis of the Tayler instability found critical currents consistent with prior work and described the instability as an edge effect, governed by curvature of the magnetic field [187]. Finally, another simulation study found that the Tayler instability occurs in Mg-based liquid metal batteries with current density $J = 300\,\mathrm{mA/cm^2}$ (a value typical for batteries being commercialized) if the battery radius exceeds 0.43 m and causes rupture if the radius exceeds 3 m [188]. Though there are economic advantages to increasing battery size, we are unaware of prototypes that large.

To summarize: The Tayler instability is a magnetohydrodynamic phenomenon that drives flow when a large axial current passes through liquid metal. Because of the magnitude of the currents involved, and because today's liquid metal battery designs have large aspect ratio, the Tayler instability may not yet affect the technology. For larger, next-generation batteries, however, the Tayler instability should be considered carefully. A variety of engineering solutions to avoid or damp the instability are now known.

7 Electro-Vortex Flow

The Tayler instability discussed in Sec. 6 is an interaction of an electrical current with the magnetic field produced by the current

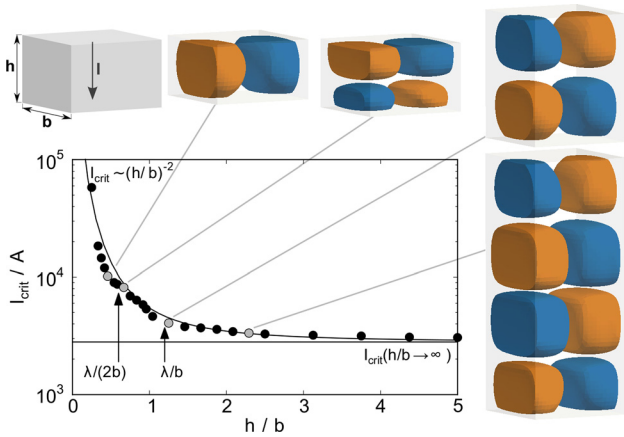

Fig. 16 Critical current for the Tayler instability depending on the aspect ratio of a cuboid with square cross section ($96 \times 96\,\mathrm{mm}^3$) filled with InGaSn ($\sigma = 3.29 \times 10^6$ S/m, $\rho = 6403\,\mathrm{kg/m}^3$, and $\nu = 3.4 \times 10^{-7}\,\mathrm{m}^2/\mathrm{s}$), determined in simulations. The insets show contours of the induced vertical magnetic field component. Adapted from Ref. [181].

itself. If condition (19) is satisfied and enough current runs, the instability drives flow even in the case of a purely axial, azimuthally symmetric current. Currents of other shapes can also interact with their own magnetic fields to produce forces. In particular, if the Lorentz force produced by self-interaction has nonzero curl, a conductive fluid flows even with arbitrarily weak currents in the absence of perturbations. The phenomenon, known as "electro-vortex flow," has been reviewed in detail [189] and is commonly studied in the context of vacuum arc remelting [111,190]. Here, we will give a brief overview and consider the implications of electro-vortex flow for liquid metal batteries.

To show that a Lorentz force with nonzero curl drives flow, we consider the conservation of momentum of an incompressible Newtonian fluid acted upon by a force per unit mass $\boldsymbol{F}$

$$\frac{\partial \boldsymbol{u}}{\partial t} + (\boldsymbol{u} \cdot \nabla)\boldsymbol{u} = -\frac{1}{\rho}\nabla p + \nu \nabla^2 \boldsymbol{u} + \boldsymbol{F}$$

Here, $\boldsymbol{u}$ is the fluid velocity. It follows that stagnant fluid ($\boldsymbol{u} = 0$) conserves momentum if and only if

$$\frac{1}{\rho}\nabla p = \boldsymbol{F} \tag{20}$$

One example, of course, is the gravitational force $\boldsymbol{F} = -g\hat{z}$, where we take $\hat{z}$ as vertical. In that case, Eq. (20) may be integrated directly, yielding the familiar fact that the hydrostatic pressure a distance h below the fluid surface is $p = \rho g h$. On the other hand, if $\nabla \times \boldsymbol{F} \neq 0$, Eq. (20) has no solution, since the curl of a gradient is always zero. In that case, we conclude that our assumption $\boldsymbol{u} = 0$ was false, that is, if a fluid is acted upon by a force $\boldsymbol{F}$ for which $\nabla \times \boldsymbol{F} \neq 0$, the fluid must flow.

If we are interested in the Lorentz force per unit volume $\boldsymbol{F} = \boldsymbol{J} \times \boldsymbol{B}$ due to interaction of an electrical current with its own magnetic field, and under the simplifying assumption that all quantities are azimuthally symmetric, it can be shown [189] that $\nabla \times \boldsymbol{F} \neq 0$ simplifies to

$$\frac{\partial B_\varphi}{\partial z} \neq 0$$

The magnetic field B_φ depends, via the Biot–Savart law, on the current density $\boldsymbol{J}$. So in azimuthally symmetric systems like cylindrical liquid metal batteries, electro-vortex flow occurs when $\boldsymbol{J}$ varies axially. In fact, it can be shown that any divergent current density in an axisymmetric system causes electro-vortex flow. One canonical example is flow driven by a current from the center of a hemisphere to the hemisphere's surface [189]. Taking the additional assumption that the resulting flow is irrotational allows analytical solution of many other cases as well. However, many are similarity solutions for which boundary conditions are evaluated at infinity, hindering their application to technological applications like liquid metal batteries.

The details of electro-vortex flow are typically studied via simulation or experiment. Flows typically converge where the current density is highest, causing the largest magnetic pressure. In azimuthally symmetric situations, the result is a poloidal circulation. Current density can be shaped by choosing electrode geometry [191] or by adding a nearby ferromagnetic object, which concentrates magnetic field lines [192]. Electro-vortex flow can cause substantial pressure and was therefore recognized as a promising mechanism for pumping liquid metals in technological applications including metals processing and nuclear cooling [193]. Subsequent efforts produced pumps that drive liquid metal in flat channels with corners [194], through Y- and Ψ-shaped junctions [195], in a winding-free pump composed of a pair of junctions [196], and centrifugally [197]. Electro-vortex flow also occurs in cylindrical steel furnaces [198].

Electro-vortex flow almost certainly occurs in typical liquid metal batteries because current diverges from the negative current collector to the casing, which serves as positive current collector. Changing the size and aspect ratio of the current collectors and electrodes can impede or promote electro-vortex flow in simulations [137]. Because electro-vortex flow is not an instability, there are no critical dimensionless parameters below which it disappears. Even small liquid metal batteries supporting gentle currents are susceptible to finite electro-vortex flow, which may make it a more important engineering consideration than the Tayler instability. In fact, an experimental device initially designed to produce the Tayler instability also drove measurable motion at currents too small for instability [199] after holes for ultrasound Doppler velocimetry probes were drilled in the current collectors. The motion stopped immediately when current was turned off, a behavior inconsistent with thermal convection; probably, electro-vortex flow was the cause. In fact, electro-vortex flow seems to suppress the Tayler instability in simulations for thin current collectors (curve $h_{CC}/D = 2$ of Fig. 17), though the Tayler instability, once it sets in, suppresses electro-vortex flow, see the $h_{CC}/D = 3$ curve and the insets in Fig. 17. Narrow current collectors and thin fluid layers produce current distributions that diverge more, and therefore, drive stronger electro-vortex flow [185]. Intermetallic solids floating at the interface between the positive electrode and electrolyte could also cause electro-vortex flow, since their conductivity is typically lower than the surrounding melt.

Electro-vortex flow also competes with thermal convection driven by Joule heating. Current diverges from the negative current collector at the top of the battery, so electro-vortex flow tends to form a poloidal roll directed inward at the top and descending along the central axis. Joule heating, on the other hand, tends to cause a poloidal roll that rises along the central axis, where current and therefore heat are concentrated. Both opposing phenomena grow stronger as current increases. In the limiting case of very high current, we would expect thermal effects to dominate, since the rate of Joule heating grows as the square of the current, whereas the work done by electro-vortex flow grows proportionally with current. Still, because both phenomena also depend on the spatial distribution of current, their competition is probably complicated and requires further study.

Davidson [111] considered the analogous problem of competition between electro-vortex flow and thermal convection in vacuum arc remelting in which current diverges from a small electrode through a hemispherical pool of molten metal. The resulting flow can be characterized with the dimensionless quantity

$$\chi = \frac{I}{2\pi\kappa}\left(\frac{\mu}{\rho}\right)^{1/2}\left(\frac{3\kappa^2}{g\alpha_T L^3 \Delta T}\right)^{3/7}$$

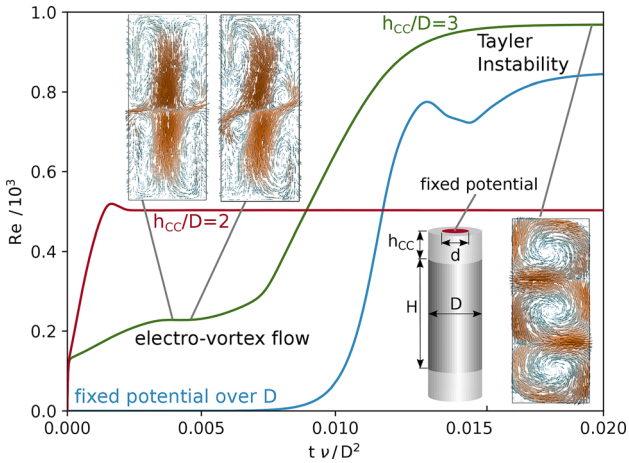

Fig. 17 Reynolds number based on the mean velocity in a cylindrical liquid metal column versus time in viscous units. The applied current density corresponds to Ha = 100, column diameter and height are ($D = 1$ m, $H = 2.4$ m). The material parameters correspond to Na at 580 °C. h_{CC} denotes the height of the current collectors, their conductivity is five times that of sodium. The centered area with fixed potential has a diameter $d = 0.5D$. The insets show velocity snapshots in a meridional plane. Adapted from Ref. [137].

where I is the current. Roughly, χ gives the ratio of the characteristic speed of electro-vortex flow to the characteristic speed of thermal convection, and we refer the reader to the original source [111] for more detail. When $\chi < 0.4$, thermal convection dominates, and fluid rises along the central axis, as expected. When $\chi > 1.4$, electro-vortex flow dominates, and fluid descends along the central axis. At intermediate values of χ, the two mechanisms have similar strength, and their competition produces more complicated flow patterns involving multiple circulating rolls. Though liquid metal batteries typically involve different sizes, geometries, and materials than remelters, χ can probably predict the relative importance of thermal convection and electro-vortex flow nonetheless, though the values $\chi < 0.4$ and $\chi > 1.4$ will likely change. However, since χ is written in terms of a fixed temperature differential ΔT, it may be a better predictor for convection driven by temperature differences at the boundaries than for convection driven by internal Joule heating.

Like other motions, electro-vortex flow can enhance battery performance by keeping each layer more chemically uniform, but can destroy a battery by rupturing the electrolyte layer. A good predictor of rupture is the Richardson number

$$\mathrm{Ri} = \frac{(\rho_2/\rho_1 - 1)gL}{\langle u \rangle^2}$$

a ratio of the gravitational energy of stratification to the kinetic energy of flow [185,188]. Here, ρ_1 is the density of the electrolyte and ρ_2 is the density of the positive electrode. Vigorous flow in an electrolyte that is nearly as dense as the electrode below it yields a small value of Ri and makes rupture likely. A similar Richardson number can be constructed for the interface between the negative electrode and the electrolyte, but rupture is less likely there because the negative electrode is often held in place by a foam current collector.

8 Summary and Future Directions

In this section, we conclude with a brief summary of the fluid mechanics of liquid metal batteries, especially thermal convection, compositional convection, Marangoni flow, and electro-vortex flow, including a few words about the importance of aspect ratio. Finally, we close with a discussion of open questions and future research directions, including richer experimental measurements, more realistic simulations, applications to battery design, size effects, temperature effects, and the role of solid separators.

8.1 Summary. We have considered the fluid mechanics of liquid metal batteries, which are made from two liquid metal electrodes and a molten salt electrolyte, without solid separators. Intended primarily for grid-scale storage, liquid metal batteries involve similar phenomena to those in technologies that were invented earlier, including aluminum smelters, aluminum refinement cells, and thermally regenerative electrochemical systems. Fluid flow may occur in the electrolyte or the positive electrode, and affects mass transfer in both layers, but is likely negligible in the negative electrode, where a metal foam hinders motion. Flow can destroy liquid metal batteries if it becomes vigorous enough to rupture the electrolyte layer. However, flow can also be beneficial. In parameter regimes common in today's liquid metal batteries, flow is likely important for preventing the formation of solid intermetallic phases, which can swell and cause electrical shorts between the positive and negative electrodes, destroying batteries. The extent of swelling depends on the density difference between intermetallic and liquid metal. Intermetallic phases are most likely to form during rapid discharge, but cannot form during charge, so rapid charging poses no danger.

In current liquid metal battery designs, the primary mechanisms driving flow include thermal convection, compositional convection, Marangoni flow, and electro-vortex flow. Because the resistivity of the electrolyte layer is four orders of magnitude higher than the electrode layers, nearly all Joule heating occurs in the electrolyte, and thermal convection is likely strongest there. The positive electrode, below the electrolyte, is usually subject to stable temperature stratification that may actually hinder flow. Thermal convection in the electrolyte layer is constrained—but slowed little or none—by the magnetic fields produced by battery currents. The low Prandtl number of the molten salt electrolyte causes its convection to have different properties than a high-Pr fluid like air.

The magnitude of Marangoni flow in liquid metal batteries is difficult to estimate because the surface tension between molten salts and liquid metals—and its variation with temperature and composition—has rarely been characterized. That said, because the electrolyte layer is thin, because the layer is subject to intense Joule heating, and because liquid metals have unusually high surface tension in vacuum, Marangoni flow along electrolyte surfaces is probably substantial.

Electro-vortex flow, driven by an electrical current interacting with its own magnetic field, is present but probably weaker than thermal convection or Marangoni flow in most liquid metal batteries. However, electro-vortex flow that may interact with other flow mechanisms can cause important effects. Current can also drive flow by interacting with external magnetic fields, though that effect is also relatively weak. Interface instabilities and the Tayler instability are unlikely in today's liquid metal battery designs, but would become crucial in larger batteries (as discussed further below). The aspect ratio of liquid metal batteries plays an important role. Given two batteries with the same capacity (and therefore same volume), the shallower and broader battery is more prone to interface instabilities, whereas the deeper and narrower battery is more prone to the Tayler instability. Interactions among mechanisms driving flow are also likely and could trigger instabilities, but little is yet known about the details of their interactions.

8.2 Open Questions and Future Directions. Much remains unknown about the fluid mechanics of liquid metal batteries, leaving many open research opportunities. First, richer experimental measurements would substantially advance the field. In experiments, measuring the flow of an opaque, high-temperature fluid is

unavoidably difficult. Ultrasound Doppler velocimetry [200] provides richer measurements than most other methods. Each transducer typically measures one velocity component at a few hundred locations along the probe's line of sight. Though a line of measurements gives much more insight into flow shape than point measurements, ultrasound data are nonetheless sparser than the two- and three-dimensional measurements commonly available via optical techniques in fluids that are transparent. (A recent review [201] of velocity measurement methods for liquid metals is also available.) Experimentalists could contribute substantially to the field by using multiple probes, either to make single-component measurements along multiple (carefully chosen) lines [199], or to make multicomponent measurements along a single line. Recent work demonstrating two-component, two-dimensional velocity measurement using phased arrays of ultrasound transducers shows great promise [202–205]. Also, no ultrasound measurements in a working, three-layer battery have been published. Instead, all measurements to date were made in a single liquid metal layer, without electrolyte or a second metal layer [120,121]. However, single-layer experimental models capture only a subset of the fluid mechanics of liquid metal batteries, including Joule heating but not heating via entropy change or heat of formation, which may have significant effects [22] and including thermal convection but not compositional convection. Directly measuring the flow in the positive electrode and the electrolyte of a functioning battery would address many open questions and is a worthy goal for experimentalists. Finally, ultrasound measurements have so far been restricted to temperatures below 230 °C, though the batteries being commercialized are solid at those temperatures. High-temperature ultrasound probes with waveguides have been demonstrated [206] and could be applied to batteries.

Second, simulation results incorporating more of the relevant physics would substantially advance the field. Simulations to date have sometimes constrained themselves to a single layer [188] and have often constrained themselves to a subset of possible flow mechanisms, for example, thermal convection [123], electro-vortex flow [137], or the combination of thermal convection and Marangoni flow [130]. These simplifications are important first steps to validate codes and build intuition for physical mechanisms at play in liquid metal batteries. Nor are the simulations undertaken trivial—low-Pr fluids are tricky and expensive to simulate, and essential material properties have been unavailable. Still, interaction among flow mechanisms is all but certain, so discovering the dynamics of liquid metal batteries and accurately forecasting their behavior will require simulations incorporating multiple mechanisms. Measuring material properties, especially the surface tensions between liquid metals and molten salts, along with their dependence on temperature and composition, would enable better-constrained simulations. Simulating three-layer liquid metal batteries including multiple flow mechanisms would be a great step forward. Among the long list of mechanisms, it seems that thermal convection, compositional convection, Marangoni flow, and electro-vortex flow are most relevant for today's liquid metal batteries. Heat of formation and entropy change may also be significant [22]. In simulations of larger batteries, surface instabilities, the Tayler instability, and forces caused by external magnetic fields may have stronger effects.

Third, richer experimental measurements and simulations incorporating more of the relevant physics would allow improved battery design. Liquid metal batteries involve a large number of design parameters (electrode materials, electrolyte material, size, shape, temperature, current density, etc.) and a large number of engineering metrics (cost, voltage, temperature, cycle life, etc.). So far, materials choices have been considered most carefully, and cost has been identified as the primary engineering metric. Still, trade-offs are common, and the technology is new enough that the long-term consequences of design choices are not always clear. For example, Li||PbSb batteries achieve higher voltage and lower cost per kWh than Li||Bi batteries [13,15], but if Li||Bi batteries last much longer because of their ability to eliminate intermetallic growth electrochemically, their lifetime cost may be lower. Improved fluid mechanical experiments and simulations might be accurate enough to predict the rate of intermetallic growth and answer the question of material choice.

Battery size is a particularly interesting design parameter for fluid mechanical investigation. Aluminum smelters are typically large, with horizontal dimensions on the order of $3\ \mathrm{m} \times 10\ \mathrm{m}$, which lowers the cost of aluminum. Similarly, liquid metal batteries might provide storage at lower cost if they were larger. For the same energy (or power), larger batteries require less container material and less power electronics, offering substantial cost reductions. However, larger batteries are more susceptible to electrolyte rupture by surface instabilities or the Tayler instability (though the aspect ratio also plays an important role). Preliminary experiments also show them to be more susceptible to shorts due to intermetallic growth. Today's prototypes are kept small (200 mm) to avoid those drawbacks, but improved understanding of the fluid mechanics might overcome them and allow larger, lower-cost batteries. In aluminum production, surface instabilities are damped by thickening the electrolyte to about 4 cm [159], at the cost of requiring more voltage—and therefore more energy—to drive current. In batteries, however, that mitigation strategy is unavailable, since the available voltage is fundamentally limited by electrode materials, and typically $\lesssim 1$ V. Improved understanding of the fluid mechanics of liquid metal batteries might reveal alternate strategies. One question of battery size has already been addressed: simulations have shown that batteries designed small enough (and with the right aspect ratio) can avoid the Tayler instability altogether [188]. Surface instabilities can probably be avoided with a similar design strategy, and simulations (or perhaps experiments) could determine the required size and shape precisely.

Fourth, liquid metal battery fluid mechanics and device designs may change radically if low-temperature chemistries are discovered. Battery prototypes being commercialized operate at 475 °C, mainly because the melting point of their molten salt electrolyte is nearly that high. Batteries stacked in large arrays can maintain that temperature by Joule heating if they are used regularly, but when unused, they require extra heat, adding cost. Reducing the operating temperature would reduce that cost and probably have greater effects on other costs. Lower temperatures would cause slower chemical kinetics of side reactions that reduce battery efficiency and corrode containers and current collectors. Lower temperatures would ease the design of seals. Much lower temperatures would allow less expensive container materials, like plastics instead of stainless steel. Thus, substantial effort is being dedicated to the search for viable low-temperature liquid metal battery chemistries [23,79,207–209]. If found, they would have significantly different material properties than today's liquid metal batteries, and therefore, give rise to significantly different fluid mechanics. For example, the lowest-temperature systems use electrolytes composed of room temperature ionic liquids instead of molten salts [208,209]. Ionic liquids, however, have typical conductivities orders of magnitude smaller than those of molten salts. Liquid metal batteries made with ionic liquids, therefore, would require much thinner electrolyte layers to produce the same voltage, and Joule heating would be still more isolated to the electrolyte layer. The relative magnitude of flow mechanisms (thermal convection, Marangoni flow, electro-vortex flow, instabilities, etc.) may also be different in low-temperature batteries. If low-temperature liquid metal batteries become possible, many practical and interesting questions of fluid mechanics will arise.

Fifth and finally, though we have focused on liquid metal batteries without solid separators, there are existing technologies [5,6] as well as proposed next-generation batteries [16,17] that include them. The presence of a solid separator radically changes the fluid mechanics and design of batteries. Without any interfaces between two different liquids, neither Marangoni flow nor surface instabilities are possible. Instead, both electrodes are subject to no-slip boundary conditions at the separator. Solid separators

eliminate the possibility of rupture due to fluid mechanics and allow electrodes to be positioned side-by-side instead of being stacked vertically. Solid separators have electrical conductivity substantially lower than molten salt—about six orders of magnitude lower than liquid metals—so heat production would be even more concentrated. High-temperature batteries using solid separators come with their own set of interesting and practical fluid mechanical questions.

The fluid mechanics of liquid metal batteries is an exciting topic, involving an increasing number of researchers and a large number of open questions. Enabling large-scale storage to make electrical grids more robust while incorporating more wind and solar generation would make a tremendous social impact. Interactions among mass transport, heat transport, multiphase flow, magnetohydrodynamics, and chemical reaction make batteries complicated and interesting. We urge and encourage researchers to focus on problems that are both practical for enabling battery technology and interesting for broadening human knowledge.

Acknowledgment

The authors are grateful to F. Stefani for comments on an early draft of the paper. Fruitful discussions with Valdis Bojarevičs, Wietze Herreman, Gerrit Horstmann, Caroline Nore, Takanari Ouchi, Donald Sadoway, Norbert Weber, and Oleg Zikanov are gratefully acknowledged.

Funding Data

- Helmholtz-Gemeinschaft Deutscher Forschungszentren (HGF) (LIMTECH).
- National Science Foundation (Award No. CBET-1552182).

Nomenclature

a_M = activity of M
$a_{M^{z+}}$ = activity of the cation of M
$a_{M(N)}$ = activity of M alloyed with N
$\mathcal{A}_g$ = interface interaction parameter
B = characteristic magnetic field strength
B_φ = azimuthal component of magnetic field
Bo = dynamic Bond number
c_p = specific heat at constant pressure
D = material diffusivity
E = voltage
E_{OC} = open circuit voltage
F = Faraday constant
$\boldsymbol{F}$ = force per unit mass
$\boldsymbol{F_L}$ = Lorentz force per unit volume
g = acceleration due to gravity
G = Galileo number
H_C = cryolite layer thickness
H_E = aluminum layer thickness
Ha = Hartmann number
I = current
I_h = horizontal perturbation current
J = current density
L = vertical thickness
L_x = x-direction size
L_y = y-direction size
L_z = z-direction size
M = alkali or earth alkali metal
Ma = thermal Marangoni number
m = azimuthal wave number
N = heavy or half metal
Nu = Nusselt number
Pm = magnetic Prandtl number
Pr = Prandtl number
Q = total heat flux
R = gas constant
R_E = ohmic resistance of the electrolyte
Ra = thermal Rayleigh number
Ra_{crit} = critical Rayleigh number for flow onset
Ra_X = compositional Rayleigh number
Re = Reynolds number
Ri = Richardson number
t = time
T = temperature
u_j = velocity component, using indicial notation
$\boldsymbol{u}$ = velocity
U = characteristic flow velocity
X = concentration of negative electrode material
X_0 = characteristic concentration
z = valency
α_T = thermal coefficient of volumetric expansion
α_X = solutal coefficient of volumetric expansion
β = Sele criterion for metal pad instability
β_{cr} = Bojarevičs–Romero criterion for metal pad instability
ΔT = characteristic temperature difference
ΔX = characteristic concentration difference
$\Delta\rho_{CE}$ = characteristic density difference
$\Delta\sigma$ = characteristic surface tension difference
$\eta_{a,a}$ = activation polarization at the anode
$\eta_{a,c}$ = activation polarization at the cathode
$\eta_{c,a}$ = concentration polarization at the anode
$\eta_{c,c}$ = concentration polarization at the cathode
η^{mn} = interface wave amplitude
κ = thermal diffusivity
μ = magnetic permeability
ν = kinematic viscosity
ρ = mass density
σ = surface tension
σ_E = electrical conductivity
τ = characteristic flow time
φ_0 = half-cell potential
φ_{00} = standard half-cell potential
ω = oscillation frequency

References

[1] Kassakian, J. G., and Schmalensee, R., 2011, *The Future of the Electric Grid: An Interdisciplinary MIT Study*, Massachusetts Institute of Technology, Cambridge, MA.
[2] Whittingham, M. S., 2012, "History, Evolution, and Future Status of Energy Storage," Proc. IEEE, **100**, pp. 1518–1534.
[3] Backhaus, S., and Chertkov, M., 2013, "Getting a Grip on the Electrical Grid," Phys. Today, **66**(5), pp. 42–48.
[4] Nardelli, P. H. J., Rubido, N., Wang, C., Baptista, M. S., Pomalaza-Raez, C., Cardieri, P., and Latva-aho, M., 2014, "Models for the Modern Power Grid," Eur. Phys. J. Spec. Top, **223**(12), pp. 2423–2437.
[5] Bones, R. J., Teagle, D. A., Brooker, S. D., and Cullen, F. L., 1989, "Development of a Ni, $NiCl_2$ Positive Electrode for a Liquid Sodium (ZEBRA) Battery Cell," J. Electrochem. Soc., **136**(5), pp. 1274–1277.
[6] Sudworth, J. L., 2001, "The Sodium/Nickel Chloride (ZEBRA) Battery," J. Power Sources, **100**(1–2), pp. 149–163.
[7] Lu, X., Li, G., Kim, J. Y., Mei, D., Lemmon, J. P., Sprenkle, V. L., and Liu, J., 2014, "Liquid-Metal Electrode to Enable Ultra-Low Temperature Sodium-Beta Alumina Batteries for Renewable Energy Storage," Nat. Commun., **5**, p. 4578.
[8] Fukunaga, A., Nohira, T., Kozawa, Y., Hagiwara, R., Sakai, S., Nitta, K., and Inazawa, S., 2012, "Intermediate-Temperature Ionic Liquid NaFSA-KFSA and Its Application to Sodium Secondary Batteries," J. Power Sources, **209**, pp. 52–56.
[9] Nitta, K., Inazawa, S., Sakai, S., Fukunaga, A., Itani, E., Numata, K., Hagiwara, R., and Nohira, T., 2013, "Development of Molten Salt Electrolyte Battery," SEI Tech. Rev., **76**, pp. 33–39.
[10] Cairns, E. J., Crouthamel, C. E., Fischer, A. K., Foster, M. S., Hesson, J. C., Johnson, C. E., Shimotake, H., and Tevebaugh, A. D., 1967, "Galvanic Cells With Fused-Salt Electrolytes," Argonne National Laboratory, Lemont, IL, Report No. ANL-7316.
[11] Kim, H., Boysen, D. A., Newhouse, J. M., Spatcco, B. L., Chung, B., Burke, P. J., Bradwell, D. J., Jiang, K., Tomaszowska, A. A., Wang, K., Wei, W., Ortiz, L. A., Barriga, S. A., Poizeau, S. M., and Sadoway, D. R., 2013, "Liquid Metal Batteries: Past, Present, and Future," Chem. Rev., **113**(3), pp. 2075–2099.
[12] Weier, T., Bund, A., El-Mofid, W., Horstmann, G. M., Lalau, C.-C., Landgraf, S., Nimtz, M., Starace, M., Stefani, F., and Weber, N., 2017, "Liquid Metal

Batteries - Materials Selection and Fluid Dynamics," IOP Conf. Ser.: Mater. Sci. Eng., **228**(1), p. 012013.
[13] Ning, X., Phadke, S., Chung, B., Yin, H., Burke, P. J., and Sadoway, D. R., 2015, "Self-Healing Li–Bi Liquid Metal Battery for Grid-Scale Energy Storage," J. Power Sources, **275**, pp. 370–376.
[14] Bradwell, D. J., Kim, H., Sirk, A. H. C., and Sadoway, D. R., 2012, "Magnesium-Antimony Liquid Metal Battery for Stationary Energy Storage," J. Am. Chem. Soc., **134**(4), pp. 1895–1897.
[15] Wang, K., Jiang, K., Chung, B., Ouchi, T., Burke, P. J., Boysen, D. A., Bradwell, D. J., Kim, H., Muecke, U., and Sadoway, D. R., 2014, "Lithium-Antimony-Lead Liquid Metal Battery for Grid-Level Storage," Nature, **514**(7522), pp. 348–350.
[16] Xu, J., Kjos, O. S., Osen, K. S., Martinez, A. M., Kongstein, O. E., and Haarberg, G. M., 2016, "Na-Zn Liquid Metal Battery," J. Power Sources, **332**, pp. 274–280.
[17] Xu, J., Martinez, A. M., Osen, K. S., Kjos, O. S., Kongstein, O. E., and Haarberg, G. M., 2017, "Electrode Behaviors of Na-Zn Liquid Metal Battery," J. Electrochem. Soc., **164**(12), pp. A2335–A2340.
[18] Kim, H., Boysen, D. A., Ouchi, T., and Sadoway, D. R., 2013, "Calcium-Bismuth Electrodes for Large-Scale Energy Storage (Liquid Metal Batteries)," J. Power Sources, **241**, pp. 239–248.
[19] Ouchi, T., Kim, H., Spatocco, B. L., and Sadoway, D. R., 2016, "Calcium-Based Multi-Element Chemistry for Grid-Scale Electrochemical Energy Storage," Nat. Commun., **7**, p. 10999.
[20] Li, H., Yin, H., Wang, K., Cheng, S., Jiang, K., and Sadoway, D. R., 2016, "Liquid Metal Electrodes for Energy Storage Batteries," Adv. Energy Mater, **6**(14), p. 1600483.
[21] Johnson, C. E., and Hathaway, E. J., 1971, "Solid-Liquid Phase Equilibria for the Ternary Systems Li(F,Cl,I) and Na(F,Cl,I)," J. Electrochem. Soc., **118**(4), pp. 631–634.
[22] Swinkels, D. A. J., 1971, "Molten Salt Batteries and Fuel Cells," *Advances in Molten Salt Chemistry*, Vol. 1, J. Braunstein, G. Mamantov, and G. Smith, eds., Plenum Press, New York, pp. 165–223.
[23] Spatocco, B. L., and Sadoway, D. R., 2015, "Cost-Based Discovery for Engineering Solutions," *Advances in Electrochemical Science and Engineering: Electrochemical Engineering Across Scales: From Molecules to Processes*, Vol. 15, R. Alikre, P. Bartlett, and J. Lipkowsi, eds., Wiley-VCH, Weinheim, Germany, Chap. 7.
[24] Drossbach, P., 1952, *Grundriß der allgemeinen technischen Elektrochemie*, Gebrüder Borntraeger, Berlin-Nikolassee, Germany.
[25] Betts, A. G., 1905, "Making Aluminium," U.S. Patent No. 795,886.
[26] Hoopes, W., 1901, "Process of the Purification of Aluminium," Alcoa, Pittsburgh, PA, U.S. Patent No. 673,364.
[27] Hoopes, W., 1925, "Electrolytically Refined Aluminum and Articles Made Therefrom," Alcoa, Pittsburgh, PA, U.S. Patent No. 1,534,315.
[28] Frary, F. C., 1925, "The Electrolytic Refining of Aluminum," Trans. Am. Electrochem. Soc., **47**, pp. 275–286.
[29] Müller, R., 1932, *Allgemeine und technische Elektrochemie*, Springer, Vienna, Austria.
[30] Hoopes, W., Edwards, J. D., and Horsfield, B. T., 1925, "Electrolytic Cell and Method of Lining the Same," Alcoa, Pittsburgh, PA, U.S. Patent No. 1,534,322.
[31] Shimotake, H., and Hesson, J. C., 1968, "New Bimetallic EMF Cell Shows Promise in Direct Energy Conversion," Atomic Energy Commission/NASA, Washington, DC, Report No. ARG-10183.
[32] von Zeerleder, A., 1955, "Aluminium," *Die technische Elektrolyse im Schmelzfluss* (Handbuch der technischen Elektrochemie, Vol. 3), G. Eger, ed., Akademische Verlagsgesellschaft Geest & Portig K.-G, Leipzig, Germany, pp. 56–364.
[33] Eger, G., ed., 1955, *Die technische Elektrolyse im Schmelzfluss*, (Handbuch der technischen Elektrochemie, Vol. 3), Akademische Verlagsgesellschaft Geest & Portig K.-G, Leipzig, Germany.
[34] Beljajew, A. I., Rapoport, M. B., and Firsanowa, L. A., 1957, *Metallurgie des Aluminiums*, Vol. 2, VEB Verlag Technik, Berlin.
[35] Gadeau, R. A., 1939, "L'aluminium Raffiné," *Reine Metalle: Herstellung, Eigenschaften, Verwendung*, A. E. van Arkel, ed., Springer, Berlin, pp. 145–167.
[36] Gadeau, R. A., 1936, "Refining of Aluminum," U.S. Patent No. 2,034,339.
[37] Hurter, H., 1937, "Improvements in or Relating to the Electrolytic Refining of Aluminium," GB Patent No. 469,361.
[38] Pearson, T. G., and Phillips, H. W. L., 1957, "The Production and Properties of Super-Purity Aluminium," Metall. Rev., **2**(1), pp. 305–360.
[39] Dube, M. C., 1954, "Extraction and Refining of Aluminium," Symposium Non-Ferrous Metal Industry, Jamshedpur, India, Feb. 1–3, pp. 127–138.
[40] Wolstenholme, G. A., 1982, "Aluminum Extraction," *Molten Salt Technology*, D. G. Lovering, ed., Springer, New York, pp. 13–55.
[41] Yan, X. Y., and Fray, D. J., 2010, "Molten Salt Electrolysis for Sustainable Metals Extraction and Materials Processing—A Review," *Electrolysis: Theory, Types and Applications*, S. Kuai and J. Meng, eds., Nova Science, New York.
[42] Edwards, J. D., Frary, F. C., and Jeffries, Z., 1930, *Aluminum and Its Production*, McGraw-Hill, New York.
[43] Singleton, E. L., and Sullivan, T. A., 1973, "Electronic Scrap Reclamation," J. Metals, **25**(6), pp. 31–34.
[44] Tiwari, B. L., and Sharma, R. A., 1984, "Electrolytic Removal of Magnesium From Scrap Aluminum," J. Metals, **36**(7), pp. 41–43.
[45] Gesing, A. J., Das, S. K., and Loutfy, R. O., 2016, "Production of Magnesium and Aluminum-Magnesium Alloys From Recycled Secondary Aluminum Scrap Melts," J. Metals, **68**(2), pp. 585–592.
[46] Gesing, A. J., and Das, S. K., 2017, "Use of Thermodynamic Modeling for Selection of Electrolyte for Electrorefining of Magnesium From Aluminum Alloy Melts," Metall. Mater. Trans. B, **48**(1), pp. 132–145.
[47] Olsen, E., and Rolseth, S., 2010, "Three-Layer Electrorefining of Silicon," Metall. Mater. Trans. B, **41**(2), pp. 295–302.
[48] Olsen, E., Rolseth, S., and Thonstad, J., 2014, "Electrorefining of Silicon by the Three-Layer Principle in a CaF_2-Based Electrolyte," *Molten Salts in Chemistry and Technology*, M. Gaune-Escard and G. M. Haarberg, eds., Wiley, Hoboken, NJ, pp. 569–576.
[49] Oishi, T., Koyama, K., and Tanaka, M., 2016, "Electrorefining of Silicon Using Molten Salt and Liquid Ally Electrodes," J. Electrochem. Soc., **163**(14), pp. E385–E389.
[50] Roberts, R., 1958, "The Fuel Cell round Table," J. Electrochem. Soc., **105**(7), pp. 428–432.
[51] Liebhafsky, H. A., 1967, "Regenerative Electrochemical Systems: An Introduction," *Regenerative EMF Cells* (Advances in Chemistry), Vol. 64, C. E. Crouthamel and H. L. Recht, eds., American Chemical Society, Washington, DC, pp. 1–10.
[52] McCully, R. C., Rymarz, T. M., and Nicholson, S. B., 1967, "Regenerative Chloride Systems for Conversion of Heat to Electrical Energy," *Regenerative EMF Cells* (Advances in Chemistry), Vol. 64, C. E. Crouthamel and H. L. Recht, eds., American Chemical Society, Washington, DC, pp. 198–212.
[53] Chum, H. L., and Osteryoung, R. A., 1980, "Review of Thermally Regenerative Electrochemical Systems Volume 1: Synopsis and Executive Summary," Solar Energy Research Institute, Golden, CO, Report No. SERI/TR-332-416.
[54] Chum, H. L., and Osteryoung, R. A., 1981, "Review of Thermally Regenerative Electrochemical Systems Volume 2," Solar Energy Research Institute, Golden, CO, Report No. SERI/TR-332-416.
[55] Yeager, E., 1958, "Fuel Cells: Basic Considerations," 12th Annual Battery Research and Development Conference, Fort Monmouth, NJ, pp. 2–4.
[56] Liebhafsky, H. A., 1959, "The Fuel Cell and the Carnot Cycle," J. Electrochem. Soc., **106**(12), pp. 1068–1071.
[57] Shearer, R. E., and Werner, R. C., 1958, "Thermally Regenerative Ionic Hydride Galvanic Cell," J. Electrochem. Soc., **105**(11), p. 693.
[58] Ciarlariello, T. A., McDonough, J. B., and Shearer, R. E., 1961, "Study of Energy Conversion Devices—Report No. 7," MSA Research Corporation, Callery, PA, Report No. MSAR 61-99.
[59] Lawroski, S., Vogel, R. C., and Munnecke, V. H., 1961, "Chemical Engineering Division Summary Report," Argonne National Laboratory, Lemont, IL, Report No. ANL-6379.
[60] Roy, P., Salamah, A., Maldonado, J., and Narkiewicz, R. S., 1993, "HYTEC—A Thermally Regenerative Fuel Cell," AIP Conf. Proc., **271**(2), pp. 913–921.
[61] Wietelmann, U., 2014, "Applications of Lithium-Containing Hydrides for Energy Storage and Conversion," Chem. Ing. Tech., **86**(12), pp. 2190–2194.
[62] Agruss, B., 1966, "Regenerative Battery," General Motors, Detroit, MI, U.S. Patent No. 3,245,836.
[63] Henderson, R. E., Agruss, B., and Caple, W. G., 1961, "Resume of Thermally Regenerative Fuel Cell Systems," *Energy Conversion for Space Power* (Progress in Astronautics and Aeronautics), Vol. 3, N. W. Snyder, ed., Academic Press, Cambridge, MA, pp. 411–423.
[64] Agruss, B., and Karas, H. R., 1962, "First Quarterly Technical Progress Report on Design and Development of a Liquid Metal Cell for the Period 1 January 1962–31 March 1962," Allison Division of General Motors Corporation, Detroit, MI, Report No. EDR 2678.
[65] Lawroski, S., Vogel, R. C., and Munnecke, V. H., 1962, "Chemical Engineering Division Summary Report," Argonne National Laboratory, Lemont, IL, Report No. ANL-6477.
[66] Austin, L. G., 1967, "Fuel Cells—A Review of Government-Sponsored Research, 1950–1964," National Aeronautics and Space Administration, Washington, DC, Report No. NASA-SP-120.
[67] Agruss, B., Karas, H. R., and Decker, V. L., 1962, "Design and Development of a Liquid Metal Fuel Cell," Aeronautical Systems Division, Dir/Aeromechanics, Flight Accessoire Lab, Wright-Patterson AFB, Dayton, OH, Report No. ASD-TDR-62-1045.
[68] Agruss, B., 1963, "Nuclear Liquid Metal Cell for Space Power," 17th Annual Power Sources Conference, May 21–23, pp. 100–103.
[69] Agruss, B., and Karas, H. R., 1967, "The Thermally Regenerative Liquid Metal Concentration Cell," *Regenerative EMF Cells* (Advances in Chemistry), Vol. 64, R. Gold, ed., American Chemical Society, Washington, DC, pp. 62–81.
[70] Kerr, R. L., 1967, "Regenerative Fuel Cells," Performance Forecast of Selected Static Energy Conversion Devices, 29th Meeting of AGARD Propulsion and Energetics Panel, G. W. Sherman and L. Devol, eds., AGARD, Air Force Aero Propulsion Laboratory and Aerospace Research Laboratories Department of the Air Force, pp. 658–715.
[71] Groce, I. J., and Oldenkamp, R. D., 1967, "Development of a Thermally Regenerative Sodium-Mercury Galvanic System—Part II: Design, Construction, and Testing of a Thermally Regenerative Sodium-Mercury Galvanic System," *Regenerative EMF Cells* (Advances in Chemistry), Vol. 64, C. E. Crouthamel, and H. L. Recht, eds., American Chemical Society, Washington, DC, pp. 43–52.
[72] Crouthamel, C. E., and Recht, H. L., eds., 1967, *Regenerative EMF Cells*, (Advances in Chemistry), Vol. 64, American Chemical Society, Washington, DC.
[73] Weaver, R. D., Smith, S. W., and Willmann, N. L., 1962, "The Sodium|Tin Liquid-Metal Cell," J. Electrochem. Soc., **109**(8), pp. 653–657.

[74] Shimotake, H., Rogers, G. L., and Cairns, E. J., 1969, "Secondary Cells With Lithium Anodes and Immobilized Fused-Salt Electrolytes," Ind. Eng. Chem. Process Des. Dev., **8**(1), pp. 51–56.
[75] Cairns, E. J., and Shimotake, H., 1969, "High-Temperature Batteries," Science, **164**(3886), pp. 1347–1355.
[76] Vogel, R. C., Proud, E. R., and Royal, J., 1968, "Chemical Engineering Division Semiannual Report," Argonne National Laboratory, Lemont, IL, Report No. ANL-7525.
[77] Lawroski, S., Vogel, R. C., Levenson, M., and Munnecke, V. H., 1963, "Chemical Engineering Division Research Highlights," Argonne National Laboratory, Lemont, IL, Report No. ANL-6766.
[78] Vogel, R. C., Burris, L., Tevebaugh, A. D., Webster, D. S., Proud, E. R., and Royal, J., 1971, "Chemical Engineering Division Research Highlights," Argonne National Laboratory, Lemont, IL, Report No. ANL-7850.
[79] Spatocco, B. L., Ouchi, T., Lambotte, G., Burke, P. J., and Sadoway, D. R., 2015, "Low-Temperature Molten Salt Electrolytes for Membrane-Free Sodium Metal Batteries," J. Electrochem. Soc., **162**(14), pp. A2729–A2736.
[80] Grube, G., 1930, *Grundzüge der theoretischen und angewandten Elektrochemie*, 2nd ed., Theodor Steinkopff, Dresden, Leipzig, Germany.
[81] Gossrau, G., 1955, "Calcium, Strontium, Barium," *Die technische Elektrolyse im Schmelzfluss*, (Handbuch der technischen Elektrochemie, Vol. 3), G. Eger, ed., Akademische Verlagsgesellschaft Geest & Portig K.-G, Leipzig, Germany, pp. 424–464.
[82] Wenger, E., Epstein, M., and Kribus, A., 2017, "Thermo-Electro-Chemical Storage (TECS) of Solar Energy," Appl. Energy, **190**, pp. 788–799.
[83] Steunenberg, R. K., and Burris, L., 2000, "From Test Tube to Pilot Plant: A 50 Year History of the Chemical Technology Division at Argonne National Laboratory," Argonne National Laboratory, Lemont, IL, Report No. ANL-00/16.
[84] Bockris, J. O., ed., 1972, *Electrochemistry of Cleaner Environments*, Plenum Press, New York.
[85] Hietbrink, E. H., McBree, J., Selis, S. M., Tricklebank, S. B., and Witherspoon, R. R., 1972, "Electrochemical Power Sources for Vehicle Propulsion," *Electrochemistry of Cleaner Environments*, J. O. Bockris, ed., Plenum Press, New York, pp. 47–97.
[86] Vogel, R. C., Levenson, M., Proud, E. R., and Royal, J., 1968, "Chemical Engineering Division Research Highlights," Argonne National Laboratory, Lemont, IL, Report No. ANL-7550.
[87] Kyle, M. L., Cairns, E. J., and Webster, D. S., 1973, "Lithium/Sulfur Batteries for Off-Peak Energy Storage: A Preliminary Comparison of Energy Storage and Peak Power Generation Systems," Argonne National Laboratory, Lemont, IL, Report No. ANL-7958.
[88] Bradwell, D., 2006, "Technical and Economic Feasibility of a High-Temperature Self-Assembling Battery," Master's thesis, Massachusetts Institute of Technology, Cambridge, MA.
[89] Bradwell, D., 2011, "LIQUID Metal Batteries: Ambipolar Electrolysis and Alkaline Earth Electroalloying Cells," Ph.D. thesis, Massachusetts Institute of Technology, Cambridge, MA.
[90] Ray, H. S., 2006, *Introduction to Melts—Molten Salts, Slags and Glasses*, Allied Publishers, New Delhi, India.
[91] Rao, Y. K., and Patil, B. V., 1971, "Thermodynamic Study of the Mg-Sb System," Metall. Trans., **2**(7), pp. 1829–1835.
[92] Leung, P., Heck, S. C., Amietszajew, T., Mohamed, M. R., Conde, M. B., Dashwood, R. J., and Bhagat, R., 2015, "Performance and Polarization Studies of the Magnesium-Antimony Liquid Metal Battery With the Use of In-Situ Reference Electrode," RSC Adv., **5**(101), pp. 83096–83105.
[93] Sadoway, D., Ceder, G., and Bradwell, D., 2012, "High-Amperage Energy Storage Device With Liquid Metal Negative Electrode and Methods," Massachusetts Institute of Technology, Cambridge, MA, U.S. Patent No. 8,268,471 B2.
[94] Ouchi, T., and Sadoway, D. R., 2017, "Positive Current Collector for Li||Sb-Pb Liquid Metal Battery," J. Power Sources, **357**, pp. 158–163.
[95] Sadoway, D. R., 2016, "Innovation in Stationary Electricity Storage: The Liquid Metal Battery," Stanford Energy Seminar, Stanford, CA, Oct. 31.
[96] Bojarevics, V., Tucs, A., and Pericleous, K., 2016, "MHD Model for Liquid Metal Batteries," Tenth PAMIR International Conference—Fundamental and Applied MHD, DIEE, Cagliari, Italy, June 20–24, pp. 638–642.
[97] Bojarevics, V., and Tucs, A., 2017, "MHD of Large Scale Liquid Metal Batteries," *Light Metals 2017* (The Minerals, Metals & Materials Series) Springer, New York, pp. 687–692.
[98] Chillà, F., and Schumacher, J., 2012, "New Perspectives in Turbulent Rayleigh-Bénard Convection," Eur. Phys. J. E, **35**(7), p. 58.
[99] Lohse, D., and Xia, K.-Q., 2010, "Small-Scale Properties of Turbulent Rayleigh-Bénard Convection," Annu. Rev. Fluid Mech., **42**(1), pp. 335–364.
[100] Ahlers, G., 2009, "Turbulent Convection," Physics, **2**, p. 74.
[101] Bodenschatz, E., Pesch, W., and Ahlers, G., 2000, "Recent Developments in Rayleigh-Bénard Convection," Annu. Rev. Fluid Mech., **32**(1), pp. 709–778.
[102] Nuclear Energy Agency, 2015, *Handbook on Lead-Bismuth Eutectic Alloy and Lead Properties, Materials Compatibility, Thermal-Hydraulics and Technologies*, Nuclear Energy Agency, Paris, France, pp. 1–950.
[103] Iida, T., and Guthrie, R. I. L., 2015, *The Thermophysical Properties of Metallic Liquids*, Vol. 1, Oxford University Press, Oxford, UK.
[104] Iida, T., and Guthrie, R. I. L., 2015, *The Thermophysical Properties of Metallic Liquids*, Vol. 2, Oxford University Press, Oxford, UK.
[105] Davidson, H. W., 1968, "Compilation of Thermophysical Properties of Liquid Lithium," National Aeronautics and Space Administration, Washington, DC, Report No. NASA TN D-4650.
[106] Sobolev, V., 2011, "Database of Thermophysical Properties of Liquid Metal Coolants for GEN-IV," SCK·CEN, Mol, Belgium, Report No. SCK·CEN-BLG-1069.
[107] Grossmann, S., and Lohse, D., 2000, "Scaling in Thermal Convection: A Unifying Theory," J. Fluid Mech., **407**, pp. 27–56.
[108] Horanyi, S., Krebs, L., and Müller, U., 1999, "Turbulent Rayleigh–Bénard Convection in Low Prandtl–Number Fluids," Int. J. Heat Mass Transfer, **42**(21), pp. 3983–4003.
[109] Jones, C. A., Moore, D. R., and Weiss, N. O., 1976, "Axisymmetric Convection in a Cylinder," J. Fluid Mech., **73**(2), pp. 353–388.
[110] Weiss, N. O., and Proctor, M. R. E., 2014, *Magnetoconvection*, Cambridge University Press, Cambridge, UK.
[111] Davidson, P. A., 2001, *An Introduction to Magnetohydrodynamics*, Cambridge University Press, Cambridge, UK.
[112] Chandrasekhar, S., 1954, "On the Inhibition of Convection by a Magnetic Field—II," Phil. Mag., **45**(370), pp. 1177–1191.
[113] Busse, F. H., and Clever, R. M., 1982, "Stability of Convection Rolls in the Presence of a Vertical Magnetic Field," Phys. Fluids, **25**(6), pp. 931–935.
[114] Burr, U., and Müller, U., 2001, "Rayleigh-Bénard Convection in Liquid Metal Layers Under the Influence of a Vertical Magnetic Field," Phys. Fluids, **13**(11), pp. 3247–3257.
[115] Aurnou, J. M., and Olson, P. L., 2001, "Experiments on Rayleigh-Bénard Convection, Magnetoconvection and Rotating Magnetoconvection in Liquid Gallium," J. Fluid Mech., **430**, pp. 283–307.
[116] Zürner,T., Liu, W., Krasnov, D., and Schumacher, J., 2016, "Heat and Momentum Transfer for Magnetoconvection in a Vertical External Magnetic Field," Phys. Rev. E, **94**(4), p. 043108.
[117] Burr, U., and Müller, U., 2002, "Rayleigh-Bénard Convection in Liquid Metal Layers Under the Influence of a Horizontal Magnetic Field," J. Fluid Mech., **453**, pp. 345–369.
[118] Moffatt, H. K., 1967, "On the Suppression of Turbulence by a Uniform Magnetic Field," J. Fluid Mech., **28**(3), pp. 571–592.
[119] Yanagisawa, T., Hamano, Y., Miyagoshi, T., Yamagishi, Y., Tasaka, Y., and Takeda, Y., 2013, "Convection Patterns in a Liquid Metal Under an Imposed Horizontal Magnetic Field," Phys. Rev. E, **88**(6), p. 063020.
[120] Kelley, D. H., and Sadoway, D. R., 2014, "Mixing in a Liquid Metal Electrode," Phys. Fluids, **26**(5), p. 057102.
[121] Perez, A., and Kelley, D. H., 2015, "Ultrasound Velocity Measurement in a Liquid Metal Electrode," J. Vis. Exp., **102**, p. e52622.
[122] Béltran, A., 2017, "MHD Natural Convection Flow in a Liquid Metal Electrode," Appl. Therm. Eng., **114**, pp. 1203–1212.
[123] Shen, Y., and Zikanov, O., 2016, "Thermal Convection in a Liquid Metal Battery," Theor. Comput. Fluid Dyn., **30**(4), pp. 275–294.
[124] Zikanov, O., and Shen, Y., 2016, "Mechanisms of Instability in Liquid Metal Batteries," Tenth PAMIR International Conference—Fundamental and Applied MHD, DIEE, Cagliari, Italy, June 20–24, pp. 522–526.
[125] Barriga, S. A., 2013, "An Electrochemical Investigation of the Chemical Diffusivity in Liquid Metal Alloys," Ph.D. thesis, Massachusetts Institute of Technology, Cambridge, MA.
[126] Janz, G. J., Dampier, F. W., Lakshminarayanan, G. R., Lorenz, P. K., and Tomkins, R. P. T., 1968, *Molten Salts: Volume 1, Electrical Conductance, Density, and Viscosity Data*, National Bureau of Standards, Washington, DC.
[127] Janz, G. J., Allen, C. B., Bansal, N. P., Murphy, R. M., and Tomkins, R. P. T., 1979, *Physical Properties Data Compilations Relevant to Energy Storage—II: Molten Salts: Data on Single and Multi-Component Salt Systems*, National Bureau of Standards, Washington, DC, pp. 1–450.
[128] Todreas, N. E., Hejzlar, P., Fong, C. J., Nikiforova, A., Petroski, R., Shwageraus, E., and Whitman, J., 2008, "Flexible Conversion Ratio Fast Reactor Systems Evaluation," Massachusetts Institute of Technology, Cambridge, MA, Report No. MIT-NFC-PR-101.
[129] Masset, P., Henry, A., Poinso, J.-Y., and Poignet, J.-C., 2006, "Ionic Conductivity Measurements of Molten Iodide-Based Electrolytes," J. Power Sources, **160**(1), pp. 752–757.
[130] Masset, P., Schoeffert, S., Poinso, J.-Y., and Poignet, J.-C., 2005, "Retained Molten Salt Electrolytes in Thermal Batteries," J. Power Sources, **139**(1–2), pp. 356–365.
[131] Köllner, T., Boeck, T., and Schumacher, J., 2017, "Thermal Rayleigh-Marangoni Convection in a Three-Layer Liquid-Metal-Battery Model," Phys. Rev. E, **95**(5), p. 053114.
[132] Xiang, L., and Zikanov, O., 2017, "Subcritical Convection in an Internally Heated Layer," Phys. Rev. Fluids, **2**(6), p. 063501.
[133] Foster, M. S., 1967, "Laboratory Studies of Intermetallic Cells," *Regenerative EMF Cells* (Advances in Chemistry), Vol. 64, C. E. Crouthamel and H. L. Recht, eds., American Chemical Society, Washington, DC, pp. 136–148.
[134] Goluskin, D., 2015, *Internally Heated Convection and Rayleigh-Bénard Convection*, Springer, New York.
[135] Shattuck, M. D., Behringer, R. P., Johnson, G. A., and Georgiadis, J. G., 1997, "Convection and Flow in Porous Media—Part 1: Visualization by Magnetic Resonance Imaging," J. Fluid Mech., **332**, pp. 215–245.
[136] Howle, L. E., Behringer, R. P., and Georgiadis, J. G., 1997, "Convection and Flow in Porous Media—Part 2: Visualization by Shadowgraph," J. Fluid Mech., **332**, pp. 247–262.
[137] Weber, N., Galindo, V., Priede, J., Stefani, F., and Weier, T., 2015, "The Influence of Current Collectors on Tayler Instability and Electro-Vortex Flows in Liquid Metal Batteries," Phys. Fluids, **27**(1), p. 014103.

[138] Davis, S. H., 1987, "Thermocapillary Instabilities," Annu. Rev. Fluid Mech., **19**(1), pp. 403–435.
[139] Schatz, M. F., and Neitzel, G. P., 2001, "Experiments on Thermocapillary Instabilities," Annu. Rev. Fluid Mech., **33**(1), pp. 93–127.
[140] Colinet, P., Legros, J. C., and Velarde, M. G., 2001, *Nonlinear Dynamics of Surface-Tension-Driven Instabilities*, Wiley-VCH, Weinheim, Germany.
[141] Prange, M., Wanschura, M., Kuhlmann, H. C., and Rath, H. J., 1999, "Linear Stability of Thermocapillary Convection in Cylindrical Liquid Bridges Under Axial Magnetic Fields," J. Fluid Mech., **394**, pp. 281–302.
[142] Morthland, T. E., and Walker, J. S., 1996, "Thermocapillary Convection During Floating-Zone Silicon Growth With a Uniform or Non-Uniform Magnetic Field," J. Cryst. Growth, **158**(4), pp. 471–479.
[143] Bratsun, D. A., and De Wit, A., 2004, "On Marangoni Convective Patterns Driven by an Exothermic Chemical Reaction in Two-Layer Systems," Phys. Fluids, **16**(4), pp. 1082–1096.
[144] Köllner, T., Schwarzenberger, K., Eckert, K., and Boeck, T., 2013, "Multiscale Structures in Solutal Marangoni Convection: Three-Dimensional Simulations and Supporting Experiments," Phys. Fluids, **25**(9), p. 092109.
[145] Köllner, T., Schwarzenberger, K., Eckert, K., and Boeck, T., 2015, "Solutal Marangoni Convection in a Hele–Shaw Geometry: Impact of Orientation and Gap Width," Eur. Phys. J.-Spec. Top, **224**(2), pp. 261–276.
[146] Jensen, K. F., Einset, E. O., and Fotiadis, D. I., 1991, "Flow Phenomena in Chemical Vapor Deposition of Thin Films," Annu. Rev. Fluid Mech, **23**(1), pp. 197–232.
[147] Craster, R. V., and Matar, O. K., 2009, "Dynamics and Stability of Thin Liquid Films," Rev. Mod. Phys., **81**(3), pp. 1131–1198.
[148] VanHook, S. J., Schatz, M. F., McCormick, W. D., Swift, J. B., and Swinney, H. L., 1995, "Long-Wavelength Instability in Surface-Tension-Driven Bénard Convection," Phys. Rev. Lett., **75**(24), pp. 4397–4400.
[149] Pearson, J. R. A., 1958, "On Convection Cells Induced by Surface Tension," J. Fluid Mech., **4**(5), pp. 489–500.
[150] Smith, K. A., 1966, "On Convective Instability Induced by Surface-Tension Gradients," J. Fluid Mech., **24**(2), pp. 401–414.
[151] Koschmieder, E. L., and Switzer, D. W., 1992, "The Wavenumbers of Supercritical Surface-Tension-Driven Bénard Convection," J. Fluid Mech., **240**(1), pp. 533–548.
[152] VanHook, S. J., Schatz, M. F., Swift, J. B., McCormick, W. D., and Swinney, H. L., 1997, "Long-Wavelength Surface-Tension-Driven Bénard Convection: Experiment and Theory," J. Fluid Mech., **345**, pp. 45–78.
[153] Welander, P., 1964, "Convective Instability in a Two-Layer Fluid Heated Uniformly From Above," Tellus, **16**(3), pp. 349–358.
[154] Walsh, W. J., Gay, E. C., Arntzen, J. D., Kincinas, J. E., Cairns, E. J., and Webster, D. S., 1971, "Lithium/Chalcogen Secondary Cells for Components in Electric Vehicular-Propulsion Generating Systems," Argonne National Laboratory, Lemont, IL, Report No. ANL-7999.
[155] Newhouse, J. M., 2014, "Modeling the Operating Voltage of Liquid Metal Battery Cells," Ph.D. thesis, Massachusetts Institute of Technology, Cambridge, MA.
[156] Scriven, L. E., and Sternling, C. V., 1964, "On Cellular Convection Driven by Surface-Tension Gradients: Effects of Mean Surface Tension and Surface Viscosity," J. Fluid Mech., **19**(3), pp. 321–340.
[157] Janz, G. J., Tomkins, R. P. T., Allen, C. B., Downey, J. R., Jr., Garner, G. L., Krebs, U., and Singer, S. K., 1975, "Molten Salts: Volume 4—Part 2: Chlorides and Mixtures—Electrical Conductance, Density, Viscosity, and Surface Tension Data," J. Phys. Chem. Ref. Data, **4**(4), pp. 871–1178.
[158] Sele, T., 1977, "Instabilities of the Metal Surface in Electrolytic Alumina Reduction Cells," Metall. Trans. B, **8B**(4), pp. 613–618.
[159] Davidson, P. A., 2000, "Overcoming Instabilities in Aluminium Reduction Cells: A Route to Cheaper Aluminium," Mater. Sci. Technol., **16**(5), pp. 475–479.
[160] Evans, J. W., and Ziegler, D. P., 2007, "The Electrolytic Production of Aluminum," *Electrochemical Engineering* (Encyclopedia of Electrochemistry), Vol. 5, A. Bard and M. Stratmann, eds., Wiley-VCH, Weinheim, Germany, pp. 224–265.
[161] Molokov, S., El, G., and Lukyanov, A., 2011, "Classification of Instability Modes in a Model of Aluminium Reduction Cells With a Uniform Magnetic Field," Theor. Comput. Fluid Dyn., **25**(5), pp. 261–279.
[162] Øye, H. A., Mason, N., Peterson, R. D., Richards, N. E., Rooy, E. L., Stevens McFadden, F. J., Zabreznik, R. D., Williams, F. S., and Wagstaff, R. B., 1999, "Aluminum: Approaching the New Millennium," J. Metals, **51**(2), pp. 29–42.
[163] Bojarevičs, V., and Romerio, V., 1994, "Long Waves Instability of Liquid Metal-Electrolyte Interface in Aluminum Electrolysis Cells: A Generalization of Sele's Criterion," Eur. J. Mech. B, **13**(1), pp. 33–56.
[164] Davidson, P. A., and Lindsay, R. I., 1998, "Stability of Interfacial Waves in Aluminium Reduction Cells," J. Fluid Mech., **362**, pp. 273–295.
[165] Sneyd, A. D., 1985, "Stability of Fluid Layers Carrying a Normal Electric Current," J. Fluid Mech., **156**(1), pp. 223–236.
[166] Zikanov, O., 2015, "Metal Pad Instabilities in Liquid Metal Batteries," Phys. Rev. E, **92**(6) p. 063021.
[167] Weber, N., Beckstein, P., Herreman, W., Horstmann, G. M., Nore, C., Stefani, F., and Weier, T., 2017, "Sloshing Instability and Electrolyte Layer Rupture in Liquid Metal Batteries," Phys. Fluids, **29**(5), p. 054101.
[168] Weber, N., Beckstein, P., Galindo, V., Herreman, W., Nore, C., Stefani, F., and Weier, T., 2017, "Metal Pad Role Instability in Liquid Metal Batteries," Magnetohydrodynamics, **53**(1), pp. 3–13.
[169] Weller, H. G., Tabor, G., Jasak, H., and Fureby, C., 1998, "A Tensorial Approach to Computational Continuum Mechanics Using Object-Oriented Techniques," Comput. Phys., **12**(6), pp. 620–631.
[170] Horstmann, G. M., Weber, N., and Weier, T., 2017, "Coupling and Stability of Interfacial Waves in Liquid Metal Batteries," e-print arXiv:1708.02159.
[171] Zikanov, O., 2017, "Shallow Water Modeling of Rolling Pad Instability in Liquid Metal Batteries," e-print arXiv:1706.08589.
[172] Tayler, R. J., 1957, "Hydromagnetic Instabilities of an Ideally Conducting Fluid," Proc. Phys. Soc. Lond. B, **70**(1), p. 31.
[173] Tayler, R. J., 1973, "The Adiabatic Stability of Stars Containing Magnetic Fields—I: Toroidal Fields," Mon. Not. R. Astron. Soc., **161**(4), pp. 365–380.
[174] Vandakurov, Y. V., 1972, "Theory for the Stability of a Star With a Toroidal Magnetic Field," Sov. Astron., **16**(2), pp. 265–272.
[175] Spruit, H. C., 2002, "Dynamo Action by Differential Rotation in a Stably Stratified Stellar Interior," Astron. Astrophys., **381**(3), pp. 923–932.
[176] Rosenbluth, M. N., 1973, "Nonlinear Properties of the Internal $m = 1$ Kink Instability in the Cylindrical Tokamak," Phys. Fluids, **16**(11), pp. 1894–1902.
[177] Freidberg, J. P., 1982, "Ideal Magnetohydrodynamic Theory of Magnetic Fusion Systems," Rev. Mod. Phys, **54**(3), pp. 801–902.
[178] Stefani, F., Weier, T., Gundrum, T., and Gerbeth, G., 2011, "How to Circumvent the Size Limitation of Liquid Metal Batteries Due to the Tayler Instability," Energ. Convers. Manage, **52**(8–9), pp. 2982 –2986.
[179] Weber, N., Galindo, V., Stefani, F., and Weier, T., 2014, "Current-Driven Flow Instabilities in Large-Scale Liquid Metal Batteries, and How to Tame Them," J. Power Sources, **265**, pp. 166–173.
[180] Shumlak, U., and Hartman, C. W., 1995, "Sheared Flow Stabilization of the m=1 Kink Mode in Z Pinches," Phys. Rev. Lett., **75**(18), pp. 3285–3288.
[181] Weber, N., Galindo, V., Stefani, F., Weier, T., and Wondrak, T., 2013, "Numerical Simulation of the Tayler Instability in Liquid Metals," New. J. Phys., **15**(4), p. 043034.
[182] Seilmayer, M., Stefani, F., Gundrum, T., Weier, T., Gerbeth, G., Gellert, M., and Rüdiger, G., 2012, "Experimental Evidence for a Transient Tayler Instability in a Cylindrical Liquid-Metal Column," Phys. Rev. Lett., **108**(24), p. 244501.
[183] Rüdiger, G., Schultz, M., and Gellert, M., 2011, "The Tayler Instability of Toroidal Magnetic Fields in a Columnar Gallium Experiment," Astron. Nachr, **332**(1), pp. 17–23.
[184] Weber, N., Galindo, V., Stefani, F., and Weier, T., 2015, "The Tayler Instability at Low Magnetic Prandtl Numbers: Between Chiral Symmetry Breaking and Helicity Oscillations," New. J. Phys., **17**(11), p. 113013.
[185] Stefani, F., Galindo, V., Kasprzyk, C., Landgraf, S., Seilmayer, M., Starace, M., Weber, N., and Weier, T., 2016, "Magnetohydrodynamic Effects in Liquid Metal Batteries," IOP Conf. Ser.: Mater. Sci. Eng., **143**(1), p. 012024.
[186] Stefani, F., Giesecke, A., Weber, N., and Weier, T., 2016, "Synchronized Helicity Oscillations: A Link Between Planetary Tides and the Solar Cycle?," Solar Phys., **291**(8), pp. 2197–2212.
[187] Priede, J., 2016, "Electromagnetic Pinch-Type Instabilities in Liquid Metal Batteries," Tenth PAMIR International Conference—Fundamental and Applied MHD, DIEE, Cagliari, Italy, June 20–24, pp. 268–273.
[188] Herreman, W., Nore, C., Cappanera, L., and Guermond, J.-L., 2015, "Tayler Instability in Liquid Metal Columns and Liquid Metal Batteries," J. Fluid Mech., **771**, pp. 79–114.
[189] Bojarevičs, V., Freibergs, Y., Shilova, E. I., and Shcherbinin, E. V., 1989, *Electrically Induced Vortical Flows*, Kluwer Academic Publishers, Dordrecht, The Netherlands.
[190] Davidson, P. A., 1999, "Magnetohydrodynamics in Materials Processing," Annu. Rev. Fluid Mech., **31**(1), pp. 273–300.
[191] Kolesnichenko, I., and Khripchenko, S., 2002, "Mathematical Simulation of Hydrodynamic Processes in the Centrifugal MHD-Pump," Magnetohydrodynamics, **38**(4), pp. 391–398.
[192] Kolesnichenko, I., Khripchenko, S., Buchenau, D., and Gerbeth, G., 2005, "Electro-Vortex Flows in a Square Layer of Liquid Metal," Magnetohydrodynamics, **41**, pp. 39–51.
[193] Denisov, S., Dolgikh, V., Mann, M. É., and Khripchenko, S., 1999, "Electrical Vortex Generation of Transit Flows Across Plane MHD Channels," Magnetohydrodynamics, **35**(1), pp. 52–58.
[194] Khripchenko, S., Kolesnichenko, I., Dolgikh, V., and Denisov, S., 2008, "Pumping Effect in a Flat MHD Channel With an Electrovortex Flow," Magnetohydrodynamics, **44**(3), pp. 303–314.
[195] Denisov, S., Dolgikh, V., Khalilov, R., Kolesnichenko, I., and Khripchenko, S., 2012, "Pumping Effect in Y- and Ψ-Shaped Channels With Π−shaped Cores," Magnetohydrodynamics, **48**(1), pp. 197–202.
[196] Dolgikh, V., and Khalilov, R., 2014, "Investigation of a Model of the Winding-Free MHD Pump With Liquid Metal Electrodes," Magnetohydrodynamics, **50**(2), pp. 187–192.
[197] Denisov, S., Dolgikh, V., Khripchenko, S., and Kolesnichenko, I., 2016, "The Electrovortex Centrifugal Pump," Magnetohydrodynamics, **52**(1–2), pp. 25–33.
[198] Kazak, O. V., and Semko, A. N., 2011, "Electrovortex Motion of a Melt in Dc Furnaces With a Bottom Electrode," J. Eng. Phys. Thermophys., **84**(1), pp. 223–231.
[199] Starace, M., Weber, N., Seilmayer, M., Kasprzyk, C., Weier, T., Stefani, F., and Eckert, S., 2015, "Ultrasound Doppler Flow Measurements in a Liquid Metal Column Under the Influence of a Strong Axial Electric Field," Magnetohydrodynamics, **51**(2), pp. 249–256.
[200] Takeda, Y., 1995, "Velocity Profile Measurement by Ultrasonic Doppler Method," Exp. Therm. Fluid Sci., **10**(4), pp. 444–453.
[201] Eckert, S., Cramer, A., and Gerbeth, G., 2007, "Velocity Measurement Techniques for Liquid Metal Flows," *Magnetohydrodynamics*, Springer, Dordrecht, The Netherlands, pp. 275–294.

[202] Büttner, L., Nauber, R., Burger, M., Räbiger, D., Franke, S., Eckert, S., and Czarske, J., 2013, "Dual-Plane Ultrasound Flow Measurements in Liquid Metals," Meas. Sci. Technol., **24**(5), p. 055302.
[203] Räbiger, D., Zhang, Y., Galindo, V., Franke, S., Willers, B., and Eckert, S., 2014, "The Relevance of Melt Convection to Grain Refinement in Al-Si Alloys Solidified Under the Impact of Electric Currents," Acta Mater., **79**, pp. 327–338.
[204] Franke, S., Räbiger, D., Galindo, V., Zhang, Y., and Eckert, S., 2016, "Investigations of Electrically Driven Liquid Metal Flows Using an Ultrasound Doppler Flow Mapping System," Flow Meas. Instrum., **48**, pp. 64–73.
[205] Nauber, R., Beyer, H., Mäder, K., Kupsch, C., Thieme, N., Büttner, L., and Czarske, J., 2016, "Modular Ultrasound Velocimeter for Adaptive Flow Mapping in Liquid Metals," IEEE International Ultrasonics Symposium (IUS), Tours, France, Sept. 18–21, pp. 1–4.
[206] Eckert, S., Gerbeth, G., and Melnikov, V. I., 2003, "Velocity Measurements at High Temperatures by Ultrasound Doppler Velocimetry Using an Acoustic Wave Guide," Exp. Fluids, **35**(6), pp. 381–388.
[207] Ashour, R. F., Yin, H., Ouchi, T., Kelley, D. H., and Sadoway, D. R., 2017, "Molten Amide-Hydroxide-Iodide Electrolyte for a Low-Temperature Sodium-Based Liquid Metal Battery," J. Electrochem. Soc., **164**(2), pp. A535–A537.
[208] Lalau, C.-C., Ispas, A., Weier, T., and Bund, A., 2015, "Sodium-Bismuth-Lead Low Temperature Liquid Metal Battery," J. Electrochem. Plating Technol., p. 4808.
[209] Lalau, C.-C., Dimitrova, A., Himmerlich, M., Ispas, A., Weier, T., Krischok, S., and Bund, A., 2016, "An Electrochemical and Photoelectron Spectroscopy Study of a Low Temperature Liquid Metal Battery Based on an Ionic Liquid Electrolyte," J. Electrochem. Soc., **163**(10), pp. A2488–A2493.